



Prospective Out-of-ecliptic White-light Imaging of Coronal Mass Ejections Traveling through the Corona and Heliosphere

Ming Xiong (熊明)^{1,2,3}, Jackie A. Davies⁴, Richard A. Harrison⁴, Yufen Zhou (周玉芬)^{1,2}, Xueshang Feng (冯学尚)^{1,2},
Lidong Xia (夏利东)⁵, Bo Li (李波)⁵, Ying D. Liu (刘颖)^{1,3}, Keiji Hayashi (林啓志)^{1,6},
Huichao Li (李会超)^{1,3}, and Liping Yang (杨利平)^{1,2}

¹ State Key Laboratory of Space Weather, National Space Science Center, Chinese Academy of Sciences, Beijing, People's Republic of China; mxiong@swl.ac.cn

² HIT Institute of Space Science and Applied Technology, Shenzhen, People's Republic of China

³ University of Chinese Academy of Sciences, Beijing, People's Republic of China

⁴ RAL Space, STFC-Rutherford Appleton Laboratory, Harwell Campus, Didcot, UK

⁵ Shandong Provincial Key Laboratory of Optical Astronomy and Solar-Terrestrial Environment, Institute of Space Sciences, Shandong University, Weihai, People's Republic of China

⁶ Institute for Space-Earth Environmental Research, Nagoya University, Japan

Received 2017 October 18; revised 2017 December 4; accepted 2017 December 5; published 2018 January 12

Abstract

The in-flight performance of the *Coriolis*/SMEI and *STEREO*/HI instruments substantiates the high-technology readiness level of white-light (WL) imaging of coronal mass ejections (CMEs) in the inner heliosphere. The WL intensity of a propagating CME is jointly determined by its evolving mass distribution and the fixed Thomson-scattering geometry. From their in-ecliptic viewpoints, SMEI and HI, the only heliospheric imagers that have been flown to date, integrate the longitudinal dimension of CMEs. In this paper, using forward magnetohydrodynamic modeling, we synthesize the WL radiance pattern of a typical halo CME viewed from an out-of-ecliptic (OOE) vantage point. The major anatomical elements of the CME identified in WL imagery are a leading sheath and a trailing ejecta; the ejecta-driven sheath is the brightest feature of the CME. The sheath, a three-dimensional (3D) dome-like density structure, occupies a wide angular extent ahead of the ejecta itself. The 2D radiance pattern of the sheath depends critically on viewpoint. For a CME modeled under solar minimum conditions, the WL radiance pattern of the sheath is generally a quasi-straight band when viewed from an in-ecliptic viewpoint and a semicircular arc from an OOE viewpoint. The dependence of the radiance pattern of the ejecta-driven sheath on viewpoint is attributed to the bimodal nature of the 3D background solar wind flow. Our forward-modeling results suggest that OOE imaging in WL radiance can enable (1) a near-ecliptic CME to be continuously tracked from its coronal initiation, (2) the longitudinal span of the CME to be readily charted, and (3) the transporting speed of the CME to be reliably determined. Additional WL polarization measurements can significantly limit the ambiguity of localizing CMEs. We assert that a panoramic OOE view in WL would be highly beneficial in revealing CME morphology and kinematics in the hitherto-unresolved longitudinal dimension and hence for monitoring the propagation and evolution of near-ecliptic CMEs for space weather operations.

Key words: magnetohydrodynamics (MHD) – methods: numerical – Sun: corona – Sun: coronal mass ejections (CMEs) – Sun: heliosphere

1. Introduction

Coronal mass ejections (CMEs) are the most energetic eruptions in the solar atmosphere and the dominant driver of severe space weather events. CMEs are traditionally defined as bright transients expelled through a coronagraph field of view (FOV) over a period of minutes to hours. The radiance (brightness) patterns of CMEs in Thomson-scattered white-light (WL) coronagraph images reflect their electron density distribution near the plane of the sky (Billings 1966). Since their discovery with the *OSO-7* coronagraph in the early 1970s (Tousey 1973), tens of thousands of CMEs have been observed by that and subsequent coronagraphs, such as the coronagraph/polarimeter (C/P) instrument onboard the *Solar Maximum Mission* (SMM; MacQueen et al. 1980), the Large Angle Spectrometric Coronagraph (LASCO) onboard the *Solar and Heliosphere Observatory* (SOHO; Brueckner et al. 1995), and the COR1 and COR2 coronagraphs onboard the *Solar-Terrestrial Relations Observatory* (STEREO; Kaiser et al. 2008). Statistical surveys of CMEs occurring over more than three solar cycles show their diverse characteristics (e.g., Hundhausen 1993; St. Cyr et al. 2000), although a “garden variety” of CMEs has emerged

from their diverse morphologies in WL imagery. This “typical” morphology of CMEs in coronagraph imagery is characterized by a three-part structure: a bright leading loop, a dark trailing low-density cavity, and a nested high-density core (e.g., Hundhausen 1993; Howard et al. 1997). The majority of CMEs undergo initial acceleration at a rate of some 100 m s^{-2} for around an hour, during which they asymptotically approach a velocity in the range of $100\text{--}1000 \text{ km s}^{-1}$ (e.g., Yashiro et al. 2004; Vršnak et al. 2007). CMEs can be categorized according to their speed: slow CMEs ($V_{\text{cme}} < 400 \text{ km s}^{-1}$), intermediate CMEs ($400 \text{ km s}^{-1} \leq V_{\text{cme}} \leq 1000 \text{ km s}^{-1}$), and fast CMEs ($V_{\text{cme}} > 1000 \text{ km s}^{-1}$). A typical CME carries a magnetic flux of 10^{23} Mx and a mass of 10^{16} g of plasma into the heliosphere (e.g., Gosling 1990; Webb & Howard 1994). The ambient solar wind flow piles up plasma and drapes magnetic field around the edges of the CME ejecta. Such piling up of plasma and draping of magnetic field forms a sheath that surrounds the moving ejecta. In this so-called snowplow scenario, the solar wind plasma that is gradually accumulated in a CME sheath substantially increases the overall mass of the propagating CME disturbance.

The bright front, dark cavity, and dense core that constitute a classic three-part CME in coronagraph imagery are generally accepted as corresponding to the coronal sheath, a magnetic flux rope (MFR), and filament material, respectively. The bright leading front is attributed to enhanced WL emission from piled-up coronal material within the coronal sheath. The interior dark cavity is suggested as being the WL manifestation of a plasma depletion region with an inherent MFR configuration (e.g., Gibson et al. 2010). The dense core is commonly considered to correspond to escaping filament material that, prior to the eruption, levitates above a photospheric polarity inversion line (PIL). This three-part structure can usually be traced directly to a small-scale progenitor of the same form confined to a solar active region or a more global-scale progenitor contained within a coronal helmet streamer. Prior to the eruption event, highly sheared magnetic arcades across the PIL are suggested to support the filament (e.g., Mikic et al. 1988; Antiochos et al. 1999; Amari et al. 2003). The magnetic field is the only coronal energy reservoir that contains sufficient energy to power a CME (Low 2001); the free magnetic energy contained within a pre-event MFR can exceed the Aly–Sturrock energy threshold (Aly 1984; Sturrock 1991). The MFR-driven CME models can account for many of the observed properties of CMEs, including their three-part density structure and post-flare arcades (e.g., Gibson & Low 1998; Manchester et al. 2004; Forbes et al. 2006). The MFR orientation and length can be inferred from the stereoscopic *STEREO* observations and using a graduated cylindrical shell (GCS) model (Thernisien et al. 2009). Upon eruption, a moving CME can potentially interact with various background structures, such as the coronal streamer belts, interplanetary corotating interacting regions (CIRs), the heliospheric plasma sheet that contains the heliospheric current sheet, and other CMEs. A multitude of physical processes governs the transfer of energy, mass, momentum, and magnetic flux to and from CMEs during their interplanetary propagation.

CMEs are the source of the most significant solar wind disturbances and consequently the source of nonrecurrent geomagnetic storms (e.g., Gosling et al. 1991; Brueckner et al. 1998; Wang et al. 2002). Magnetic clouds (MCs) are an important subset of CMEs, whose fraction decrease from nearly 100% at solar minimum to 15% at solar maximum (Richardson & Cane 2004). Burlaga et al. (1981) first discovered MCs in situ measurements. They are identified by a high magnetic field strength accompanied by a smooth rotation (e.g., south to north or east to west) in the field direction, low ion temperature, and low plasma β (typically less than 0.1). The rotation of the magnetic field inside an MC is suggestive of a coherent MFR geometry (e.g., Burlaga et al. 1981; Lepping et al. 1990; Hu & Sonnerup 2002). The occasional presence of counterstreaming electrons implies that both footpoints of the MFR are still rooted on the Sun (e.g., Gosling et al. 2001; Crooker & Horbury 2006). The decreasing flow speed during the passage of an MC suggests its continuous expansion as it propagates through the inner heliosphere. MC passage by Earth usually lasts between 7 and 48 hr, with an average of around 21 hr (Lepping et al. 2006).

A cause-and-effect connection between solar eruptions and disturbances observed at Earth has been convincingly established with milestone advances in heliospheric imaging. WL imaging at large solar elongations was performed (from early 2003 until its deactivation in 2011) by the Solar Mass Ejection

Imager (SMEI; Eyles et al. 2003) onboard the *Coriolis* spacecraft and (since the end of 2006) by the heliospheric imagers (HI1 and HI2; Howard et al. 2008; Eyles et al. 2009) onboard *STEREO* (Kaiser et al. 2008). The Sun Earth Connection Coronal and Heliospheric Investigation (SECCHI) package on each *STEREO* spacecraft comprises five telescopes: HI1, HI2, the aforementioned COR1 and COR2 coronagraphs, and an extreme ultraviolet imager (EUVI); between them, the FOVs of these instruments cover a broad range of heliocentric distances, from the solar surface to $318 R_{\odot}$ in the plane of the sky (POS). Using *STEREO*/SECCHI, a CME can be imaged from its initiation in the inner corona all the way out to 1 au and beyond (e.g., Harrison et al. 2008; Davies et al. 2009; Davis et al. 2009; Liu et al. 2010; DeForest et al. 2011, 2013; Möstl et al. 2011; Liu et al. 2013). By exploiting this unique instrument suite, DeForest et al. (2013), in particular, could associate specific elements of a CME’s in situ anatomy with features in the pre-eruptive coronal structures, as well as tracking the mass and kinetic energy of the CME as it crossed the inner solar system. The term “CME” was traditionally defined in terms of transients that occur within $30 R_{\odot}$, the outer limit of the FOV of the LASCO C3 coronagraph. Transients beyond the heliocentric distance of $30 R_{\odot}$ were traditionally classified as interplanetary CMEs (ICMEs). However, since the launch of *STEREO*, in particular, the two terms “CME” and “ICME” have increasingly become unified under the term “CME.” Moreover, the term “CME” has, over that time, come to imply the complete propagating transient observable in WL and/or EUV, including the ejecta, surrounding sheath material, and any other solar wind or coronal material entrained en route (DeForest et al. 2013). However, even with the stereoscopic imaging capabilities of the twin *STEREO* spacecraft, CMEs may have no easily identifiable signatures to locate their source regions on the Sun. Such a CME, with no apparent solar surface association in EUV wavelengths, has been termed a stealth CME (Robbrecht et al. 2009; Howard & Harrison 2013). The missing CMEs in WL observation are ascribed to an inappropriate viewing geometry and/or insufficient temporal cadence of the WL imager. The detectability of a CME in WL depends on both its electron density distribution and viewing geometry, because the WL signatures result from the Thomson scattering of sunlight by the free electrons of the CME (e.g., Vourlidas & Howard 2006; Howard & Tappin 2009; Xiong et al. 2013a). Thomson-scattering geometry is generally described with reference to the so-called Thomson sphere, the locus of points corresponding to perpendicular scattering; the Sun and the imager are at either end of one diameter of the Thomson sphere (Vourlidas & Howard 2006). Hence, both the viewing perspective of the observing WL imager and the spatial location of the CME plasma (relative to the Thomson-scattering sphere) must be considered when analyzing the detectability of CMEs in WL (Xiong et al. 2013a, 2013b). An edge-on view of a CME close to the Sun collects many more Thomson-scattered photons than a head-on view. Because the *STEREO* spacecraft orbit within the ecliptic, the longitudinal dimension of CMEs is integrated in *STEREO*/HI imagery. The determination of CME kinematics, and propagation direction in particular, is still riddled with uncertainties, particularly when viewed at large elongations (Vourlidas & Howard 2006; Howard & Tappin 2009; Davies et al. 2012; Howard & DeForest 2012; Xiong et al. 2013a, 2013b). Because of the effect of the Thomson-scattering geometry, CMEs that

propagate in or near the ecliptic plane would be clearly imaged in WL from an OOE viewpoint.

The WL imaging of the corona and heliosphere is considered an indispensable element of the scientific payload of the upcoming *Parker Solar Probe* (*PSP*; Fox et al. 2016) and *Solar Orbiter* (*Solo*; Muller et al. 2013) missions, as well as a number of other proposed mission concepts. The launch dates of *PSP* and *Solo* are currently scheduled for 2018 and 2019, respectively. A gravity assist from Venus is repeatedly used to adjust the elliptical orbits of *PSP* and *Solo*. The parameters of the prescribed *PSP* orbit are perihelion 0.04 au, apohelion 0.73 au, inclination 3.4° , and period 88 days. The orbital parameters of *Solo* are listed as perihelion 0.28 au, apohelion 0.8–0.9 au, inclination 0° – 36° , and period 150 days. *Solo* hosts multiple remote-sensing instruments, including the Multi-element Telescope for Imaging and Spectroscopy (METIS) coronagraph, which images in WL and UV, and the WL heliospheric imager (*Solo*-HI). Only a single imager is carried on *PSP*: the WL Wide-field Imager for Solar Probe (WISPR; Vourlidas et al. 2016). METIS, *Solo*-HI, and WISPR will have an unprecedented high-resolution view of the corona and heliosphere in WL at perihelion. Unprecedented WL imaging from a future OOE spacecraft, following from *Solo* but at a much greater inclination $\theta_{s/c} > 36^\circ$, would be scientifically invaluable. Such proposed OOE mission concepts include the Solar Polar Imager (SPI; Liewer et al. 2008), POLAR Investigation of the Sun (POLARIS; Appourchaux et al. 2009), Solar Polar ORbit Telescope (SPORT; Wu et al. 2011; Xiong et al. 2016), and InterHelioProbe (Kuznetsov et al. 2016). Lessons in how to optimize a prospective solar polar orbiting mission should be learned from *Solo* and also from the historic *Ulysses* mission. Using Jupiter swing-by, *Ulysses* reached an ultimate OOE orbit with inclination 80° , perihelion 1.35 au, apohelion 5.4 au, and period 6.2 yr (Wenzel et al. 1992). Without any imaging instrumentation, the *Ulysses* payload included particle/species detectors and radio/plasma-wave antennas. As the only truly OOE mission to orbit the Sun, *Ulysses* provided the first in situ measurements of the background solar wind structures (McComas et al. 2000) and transient CMEs (Gosling et al. 2001) at virtually all heliographic latitudes. Measurements from the OOE *Ulysses* mission and other in-ecliptic spacecraft were combined to provide in situ measurements of CMEs at significantly different latitudes and distances from the Sun; simultaneous in situ measurements of one specific CME from *Ulysses* and other in-ecliptic spacecraft (i.e., *WIND*, *ACE*) revealed that the CME suffered a substantial distortion during its interplanetary propagation (e.g., Gosling et al. 1994; Hammond et al. 1995). A truly OOE spacecraft mission with a WL imaging capability would resolve the tantalizing mystery as to how solar activity drives heliospheric variability in three dimensions (3D). However, any potential solar polar mission would be technologically challenging and financially costly, because the resources (such as mass, power, memory, and telemetry rate) needed to build and operate an OOE spacecraft, in particular, are at a premium. Either planetary gravity assists or solar sail propulsion has to be considered to achieve a high orbital inclination (Xiong et al. 2017). A trade-off between the inclination of a spacecraft in a solar polar orbit and its payload mass has to be considered in terms of a cost-benefit analysis.

Continuous multi-viewpoint WL observations of CMEs from Sun to Earth became a reality in the *STEREO* era. The

radiance pattern of a CME imaged by a wide-field WL imager depends significantly on the host spacecraft’s perspective. Synthetic WL signatures generated via numerical forward magnetohydrodynamic (MHD) modeling can enhance the science value of WL photometric observations, guide the scientific definition of solar and interplanetary exploration, and, in particular, justify WL coronagraph and heliospheric imagers aboard any potential OOE heliospheric mission. As a logical continuation to our previous studies that involved MHD modeling of ecliptic disturbances viewed from an in-ecliptic perspective (Xiong et al. 2013a, 2013b), OOE perspectives of 3D CIRs and CMEs are quantitatively analyzed in Xiong et al. (2017) and this paper, respectively. Our procedure for the forward modeling of Thomson-scattering WL is elaborated in Section 2 of Xiong et al. (2017). A typical halo CME with its intrinsic MFR, occurring on 1997 November 4, is numerically simulated using the CESE-MHD model (Feng et al. 2010; Zhou et al. 2012). The simulated 3D distribution of electron density is used, through the application of classic Thomson-scattering theory (Billings 1966; Vourlidas & Howard 2006; Howard & Tappin 2009; Xiong et al. 2013a), to generate synthetic 2D WL images from a number of widely distributed viewpoints in the inner heliosphere. Section 2 presents the background solar wind in the corona and heliosphere. The 3D density distribution and 2D WL radiance patterns of the modeled CME are presented in Sections 3 and 4, respectively. The scientific importance of OOE WL imaging and the outlook for an OOE spacecraft mission are discussed in Section 5.

2. Background Bimodal Solar Wind Streams in the Corona and Heliosphere

The inner heliosphere is permeated with supersonic and magnetized solar wind emanating from the Sun. The bimodal solar wind structure serves as the background medium through which CME disturbances propagate. An observed synoptic photospheric magnetogram, coupled with the analytic 1D Parker solar wind solution in a spherical symmetry, prescribes the initial conditions used to drive our 3D CESE-MHD model until the self-consistent numerical solution of the 3D solar wind flows relaxes to a steady state. The simulated density distribution of the steady solar wind is shown at various cross-sections in Figure 1. The global bimodal background solar wind structures at solar minimum are reproduced, with a slow wind emanating near the equator (at a speed of about 350 km s^{-1}) and a fast wind emanating at high latitudes (exceeding 600 km s^{-1}). The simulated local solar wind parameters are checked against in situ measurements from *ACE* at the L1 point and *Ulysses* along its polar orbit (Zhou et al. 2012). The simulated 3D density distribution in the corona is visualized as 3D isosurface volumes in Figure 2. The viewing perspectives in Figure 2 are defined in terms of θ_{axis} and ϕ_{axis} , with the subscript “axis” indicating a line-of-sight (LOS) direction along the center of the viewing FOV. Coronal streamers are the brightest feature of steady coronal WL emission. The conspicuous brightness of coronal streamers is ascribed to the confinement of dense plasma by closed magnetic field lines. For most of the solar cycle, streamers occupy the same latitudinal extent as chromospheric filaments projected onto the solar disk. As well as several filaments, a photospheric magnetic PIL usually lies underneath the coronal streamers (Zhao et al. 2005). Large-scale stable streamers are intimately linked to the same large-scale photospheric magnetic

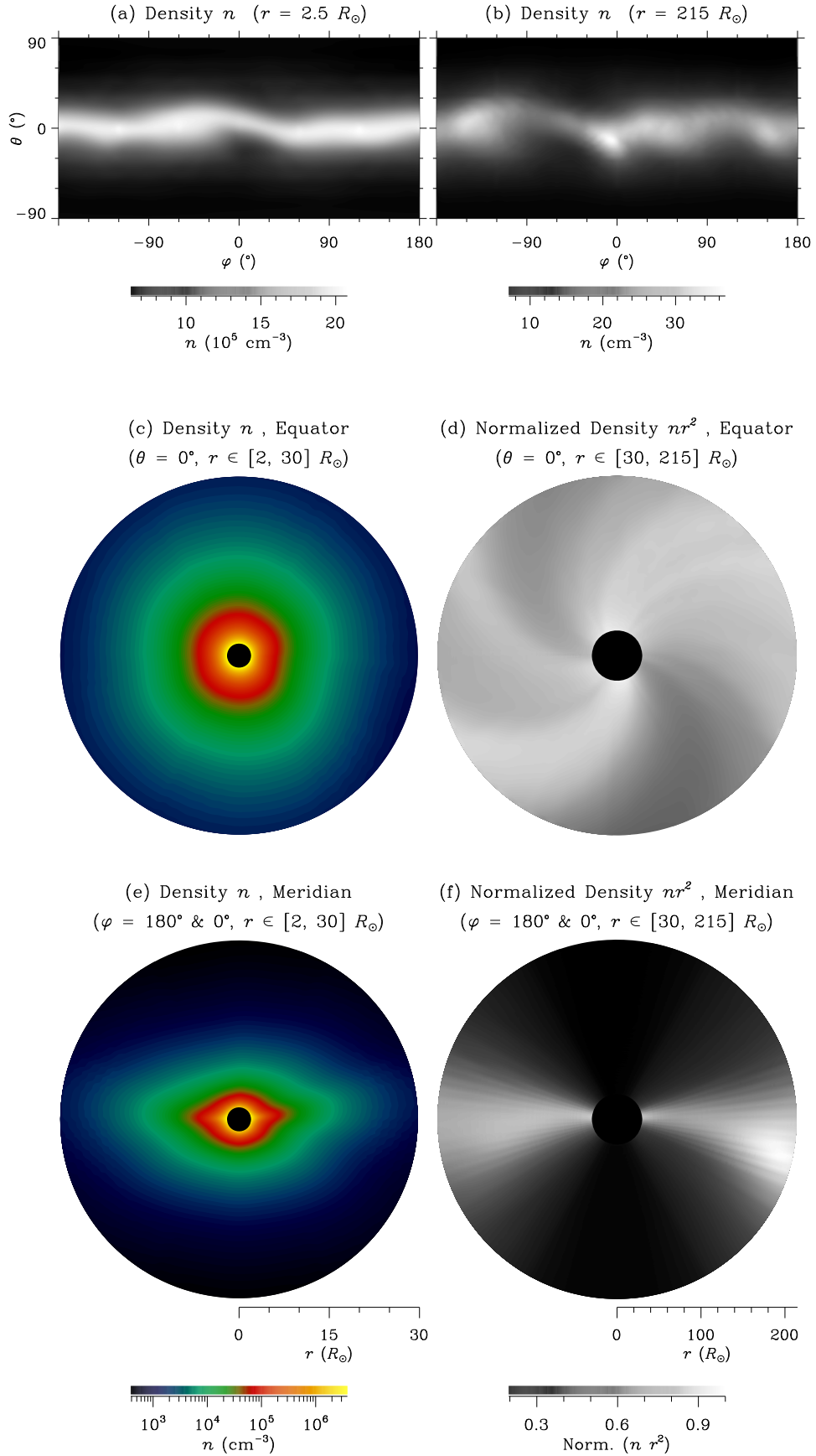


Figure 1. Distribution of the proton density n on a Sun-centered sphere (panels (a) and (b)), in the equatorial plane (panels (c) and (d)), and in the plane of the central meridian as viewed from Earth (panels (e) and (f)) in a coordinate system defined by radius r , latitude θ , and longitude φ . Panels (a), (c), and (e) are at coronal altitudes; panels (b), (d), and (f) are at heliosphere altitudes. The interplanetary density, n , is normalized as $n r^2$ in panels (d) and (f).

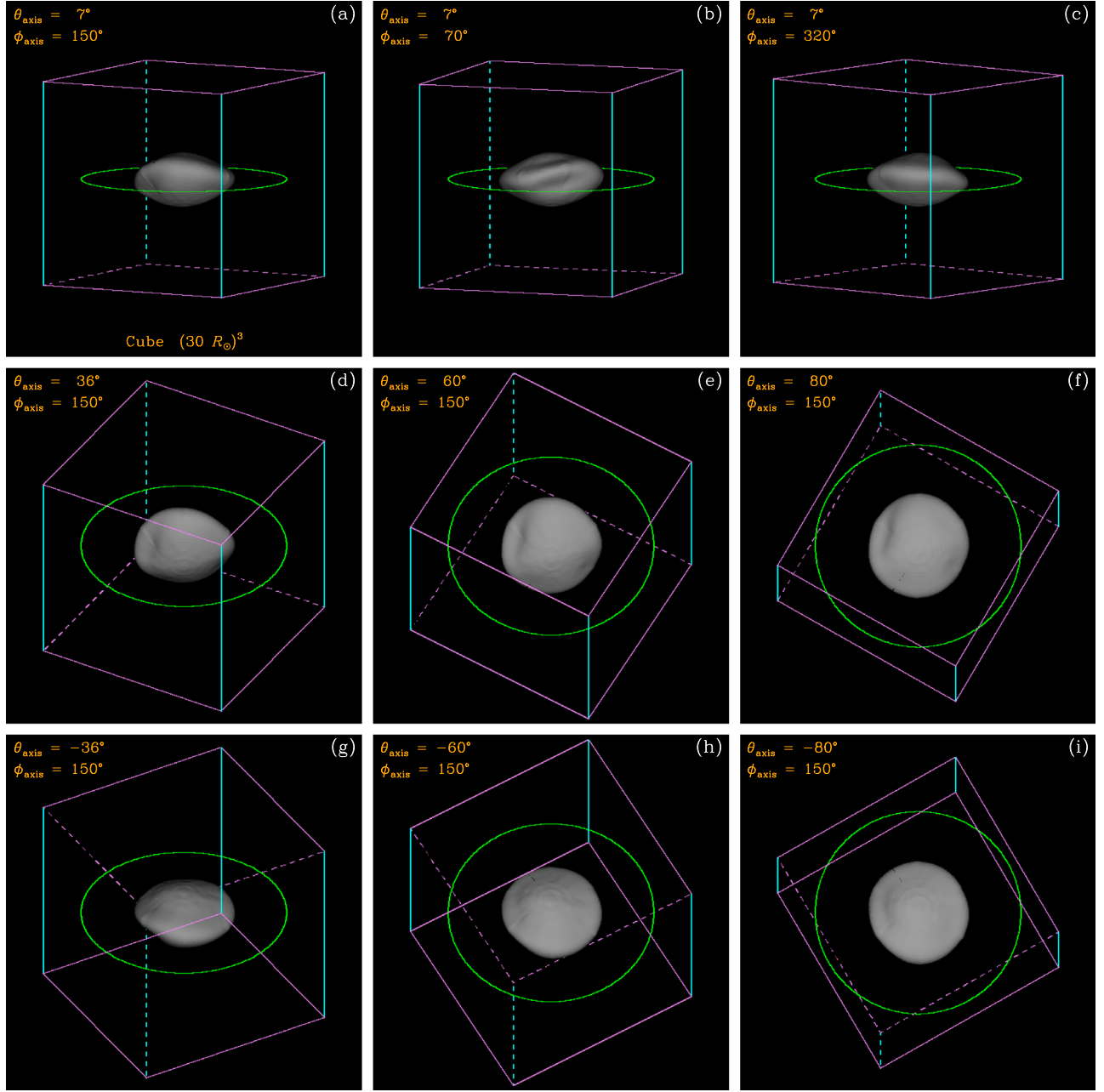


Figure 2. The 3D isosurfaces of the ambient coronal density n , viewed from a number of different vantage points. These vantage points, defined by θ_{axis} and ϕ_{axis} , are in or near the ecliptic plane for panels (a)–(c), at northern latitudes for panels (d)–(f), and at southern latitudes for panels (g)–(i). The green circle in each panel corresponds to $30 R_{\odot}$ in the ecliptic.

configuration that gives rise to large filaments. Under solar minimum conditions, as in our simulation, the 3D morphology of coronal streamers can be described by a 3D elliptical sphere (Figure 2). At lower latitudes, around the equator, a helmet streamer in quasi-stable equilibrium is stretched by the adjoining solar wind. At high latitude, the high-speed solar wind outflows along the open magnetic field configuration and stretches the coronal magnetic field lines into an Archimedean-like spiral. The gradual compression between fast and slow streamers can form large-scale CIRs in the heliosphere. Each heliospheric CIR is morphologically characterized as a 3D spiral surface, as visualized in Figure 3. The density n in Figure 3 is scaled with an r^2 falloff, as the solar wind propagates near-radially outward from the Sun. The different solar wind flows sampled at 1 au are statistically associated

with the different solar source regions in terms of coronal holes, active regions, and the quiet Sun. The photospheric footpoints of interplanetary solar wind parcels can be traced using an empirical two-step mapping procedure (Neugebauer et al. 1998, 2002) and the more sophisticated data-driven MHD models (e.g., Groth et al. 2000; Tóth et al. 2005; Feng et al. 2010). In our simulated data, coronal streamers and heliospheric CIRs are identified as different-density isosurfaces. For corona streamers, the smooth elliptic isosurface at solar minimum, shown in Figure 2, is distorted into a highly irregular surface at solar maximum (Xiong et al. 2017). The spiral isosurfaces that characterize heliospheric CIRs at solar minimum, shown in Figure 3, are warped into complicated twisted surfaces at solar maximum (Xiong et al. 2017). Such a solar cycle modulation in the morphology of the solar wind

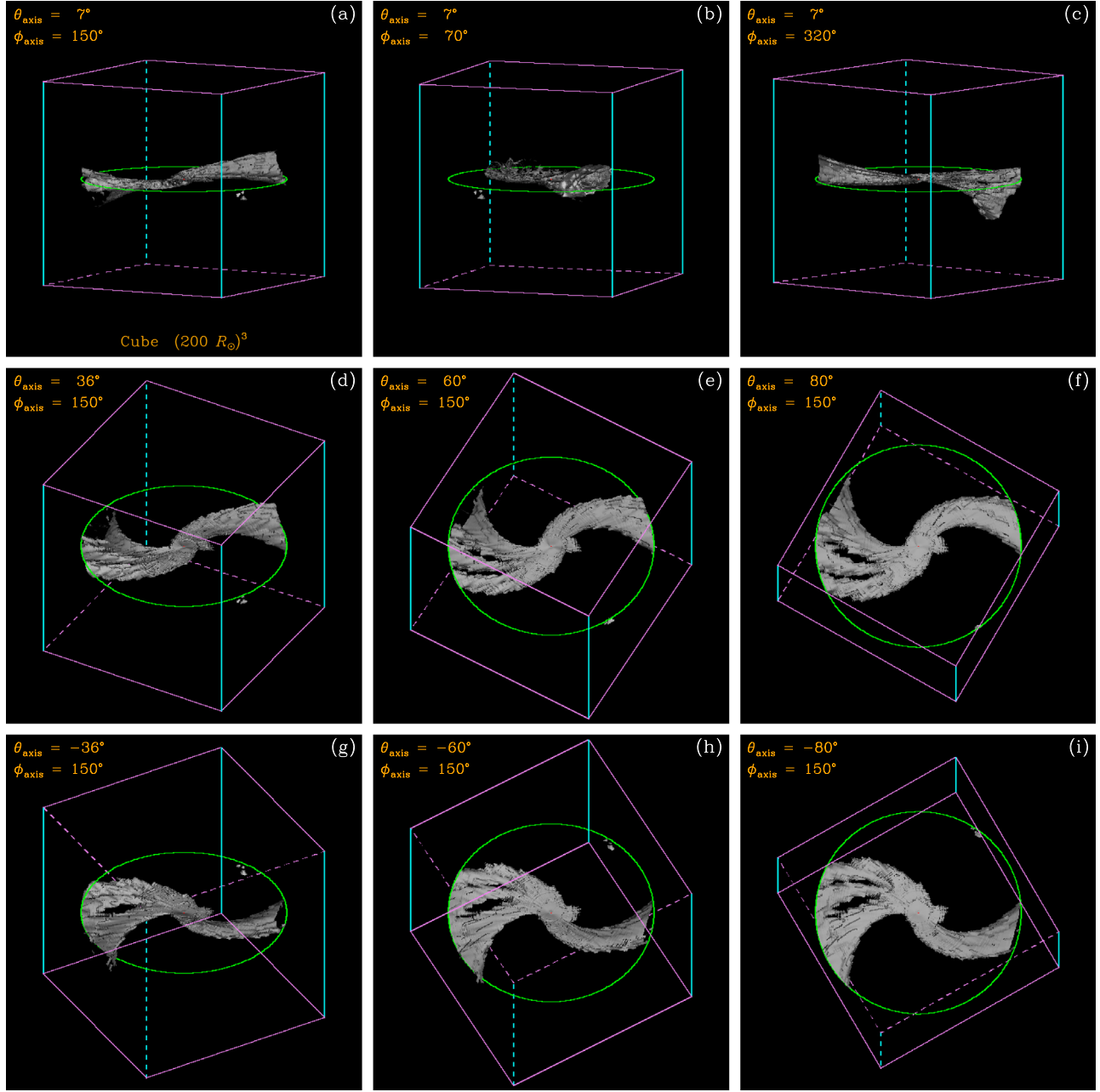


Figure 3. The 3D isosurfaces of the normalized ambient interplanetary density $n r^2$, viewed from a number of different vantage points. The green circle in each panel corresponds to $200 R_{\odot}$ in the ecliptic.

mass distribution is due to the change in the density and speed distributions at the solar source surface. At solar minimum, the background solar wind configuration is bimodal, with fast streams emanating from the polar coronal holes and slow streams emanating near the equator. At solar maximum, both slow and fast streams emerge at nearly all heliographic latitudes.

The coronal streamers that confine the high-density plasma at both solar maximum and solar minimum are readily revealed in images of total WL radiance from various 3D perspectives. As can be seen in Figure 4, the 2D WL manifestation of 3D streamer morphology at solar minimum is elliptical when viewed from an in-ecliptic perspective and circular when

viewed from an OOE perspective. Such a transition from an ellipse to a circle is smooth and continuous with increasing absolute latitude $|\theta_{s/c}|$. In contrast, the irregular 3D density ridges seen at solar maximum are imaged in 2D as a single protruding bright feature (Xiong et al. 2017). The more irregular behavior of coronal streamers imaged in 2D WL at solar maximum is a clear implication of the more complex distribution of the 3D coronal density. Estimating the density structure of the solar corona from 2D WL coronagraph images is hugely challenging. A global map of coronal structure, at a height where the coronal magnetic field becomes approximately radial ($\geq 3 R_{\odot}$), can be inferred using the qualitative

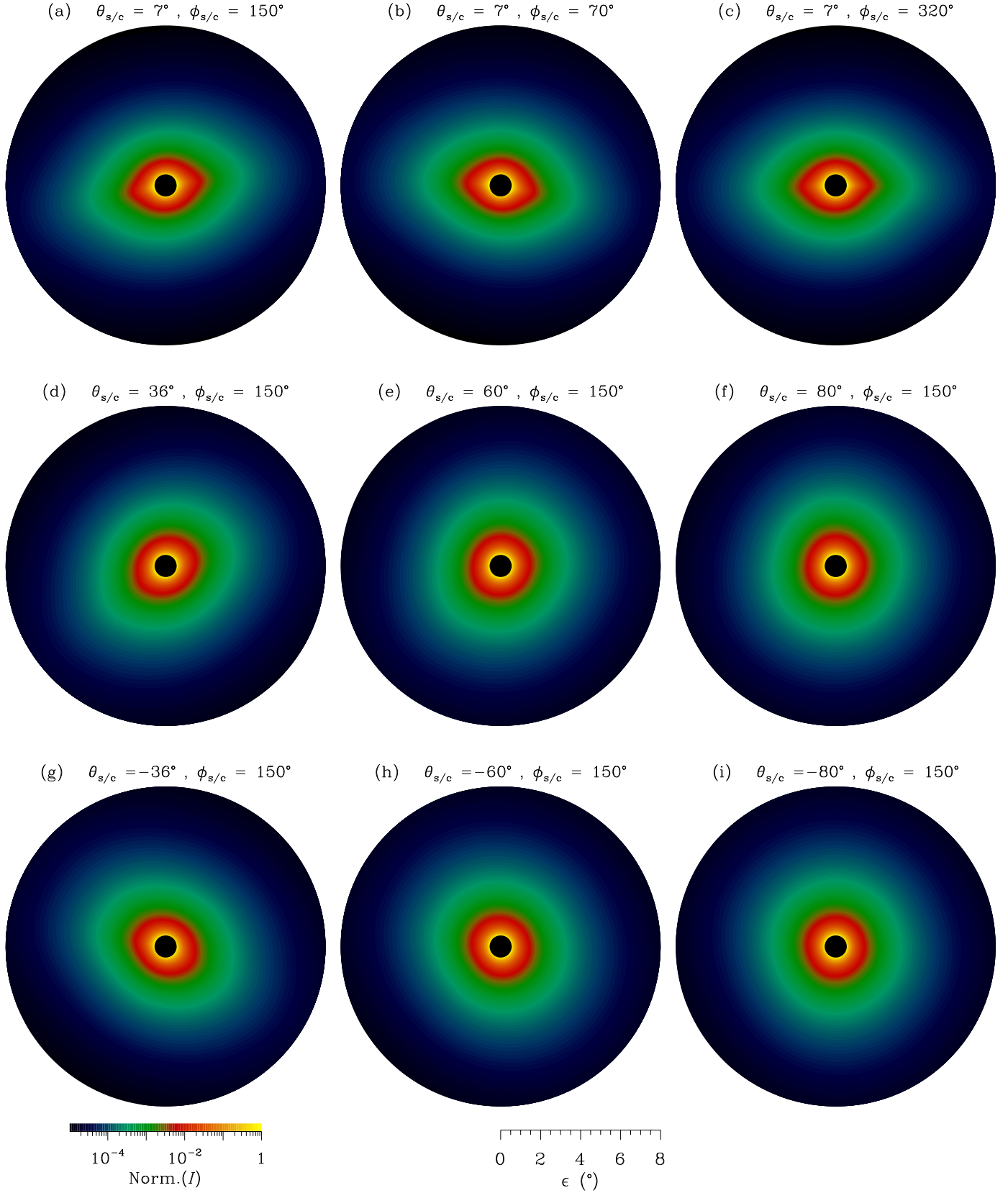
White-Light Corona Viewed from an Imager at $r_{s/c} = 215 R_{\odot}$ 

Figure 4. The WL radiance I of the ambient corona in the elongation range $\epsilon \in [0.5^\circ, 8^\circ]$, theoretically calculated for a number of $\theta_{s/c} - \phi_{s/c}$ viewpoints as prescribed in Figure 2. This elongation range corresponds to a distance range of $2\text{--}30 R_{\odot}$ in the POS.

solar rotational tomography (QSRT) technique (Morgan et al. 2012). The QSRT technique applies a suitable background subtraction and normalizing radial gradient filter to WL radiance images from the *SOHO*/LASCO C2 data archive in order to generate the distribution of coronal streamers over a full solar cycle.

3. 3D Density Distribution of CMEs in the Corona and Heliosphere

CMEs are associated with the large-scale release of plasma and magnetic field from the corona into the heliosphere and are the major cause of space weather. The causal link between the eruption of CMEs at the Sun and their resultant geospace disturbances through the tracking of their interplanetary propagation can be studied via an adaptive parallel high-performance space weather modeling infrastructure (Tóth et al. 2005; Feng et al. 2015). In this paper, the time-dependent CESE-MHD numerical modeling scheme is used to self-consistently reproduce the post-eruption and interplanetary evolution of a halo CME occurring on 1997 November 4 (Feng et al. 2010; Zhou et al. 2012). The CME at solar minimum is assumed to arise from the evolution of a spheromak magnetic structure with a high-speed, high-pressure, and high-plasma-density plasmoid inside solar active region AR8100. The CME carried an estimated total energy of 1.75×10^{32} erg and disturbed the background solar wind described in Section 2. Constrained by magnetograph observations at the photosphere and in situ particle measurements at 1 au, our numerical model reproduces the 4D global distribution (3D in space and 1D in time) of the MHD parameters (density n , speed v , magnetic field B , temperature T) throughout the inner heliosphere (Zhou et al. 2012).

The simulated MFR is initially injected outward from a heliographic latitude and longitude of 14° south and 34° west, respectively; this location corresponds to the position of a solar flare, observed at 0554 UT on 1997 November 4, that was associated with the halo CME. In our simulation, the pre-CME evolution in the low corona corresponds to an emerging MFR underneath an existing coronal streamer. A stable streamer-MFR system results from the static equilibrium between two competing forces (Chen 1989; Chen et al. 2006): (1) a lifting force provided by the azimuthal current inside the rope and its mirroring counterpart below the photosphere and (2) a restraining force produced by the background magnetic potential field. A stable MFR in the low corona is thought to be associated with a dark cavity in WL coronal emission, as the plasma is virtually evacuated from inside the MFR. Other features that signify the existence of an MFR prior to CME launch include a hot channel in EUV in the SDO/AIA 131 Å wavelength (Cheng et al. 2011). For the MFR-driven CME simulated in this paper, the overlying coronal magnetic flux inside the coronal streamer is too weak to restrain the emerging strong MFR. For the CME onset phase in the corona, the 2D density distribution in the meridional and ecliptic planes is shown in Figure 5. The slowly rising MFR stretches the surrounding magnetic field lines, resulting in expansion of the host streamer. The initial ascending MFR and the ensuing swelling of the coronal streamer are characteristic observational precursors of CME eruption. The overlying closed coronal field lines, bound to the Sun, are stretched and drape around the rising MFR as a coronal sheath. Multiple closed magnetic

structures inside the coronal sheath are carried ahead of the rising MFR outward into the heliosphere. Figure 6 presents 3D isosurfaces of the CME-disturbed coronal density as viewed from a number of different vantage points. The coronal isodensity surface, with an ellipsoidal shape, is intersected by the dome-like sheath at its round flank. At the sheath flank, the coronal mass is swept up and compressed into protruding high-density ridges. An aggressively rising altitude of the sheath dome, an expanding angular span of the sheath flank, and ridges of increasingly accumulated density characterize the temporal evolution of the coronal density during the eruption of an energetic CME. These expanding density ridges around the coronal density isosurface are only identifiable from an OOE viewing angle (Figures 6(d)–(i)). Such coronal density ridges, as a characteristic signature of CME eruption, are nearly indistinguishable from various ecliptic perspectives, particularly at solar minimum (Figures 6(a)–(c)).

The MFR-driven CME rapidly expands as it propagates outward near the Sun. Soon after, compression starts to reduce this expansion until a pressure balance is established. As the super-Alfvénic MFR propagates outward through the high corona, it generates a strong fast forward MHD shock wave. The MFR-driven shock usually extends far ahead of the MFR, and the shock geometry can be significantly modified by the structure of the background solar wind. The ambient solar wind plasma is picked up, compressed, and heated inside a solar wind sheath. Our usage of the terms “coronal sheath” and “wind sheath” follows that of DeForest et al. (2013), who distinguished these different regimes schematically in their Figure 5. The coronal sheath and wind sheath, which combine to form a compound sheath ahead of the MFR, are distinguishable on the basis of their in situ suprathermal electron signatures. The wind sheath can be identified by virtue of its field lines being connected to the Sun at only one end, with only small regions of counterstreaming electrons; the coronal sheath contains a transition between a regime in which field lines are primarily connected at one end and a regime in which both ends of the field lines are connected to the Sun, the latter regime being associated with asymmetric fluxes of counterstreaming electrons. The compound sheath has a much smaller magnetic field and a much wider angular span than its driving MFR, as shown in Figures 5 and 7. Figure 7 depicts the CME-disturbed density and magnetic field in the meridian and equator planes of the heliosphere. The sheath ahead of the near-ecliptic MFR has a 3D dome-like geometry extending to high latitudes in both the northern and southern hemispheres of the heliosphere (Figures 7(c) and (d)). Figure 8 gives the 3D isosurfaces of the normalized CME-disturbed heliospheric density $n r^2$ as viewed from a number of different vantage points. Because CIRs at solar minimum are much narrower and weaker than those at solar maximum (Xiong et al. 2017), interplanetary CME propagation at solar minimum is much simpler with less interference from CIRs.

Throughout CME propagation toward Earth, the overall mass of the CME increases via snowplow pickup of the surrounding solar wind plasma. Because the plasma in the wind sheath is being accumulated en route from the corona (Figure 5), the wind sheath begins to dominate the CME front in the heliosphere (Figure 7). The ecliptic solar wind encountered by the MFR-driven shock is denser and slower compared to the higher-latitude solar wind. Hence, the mass

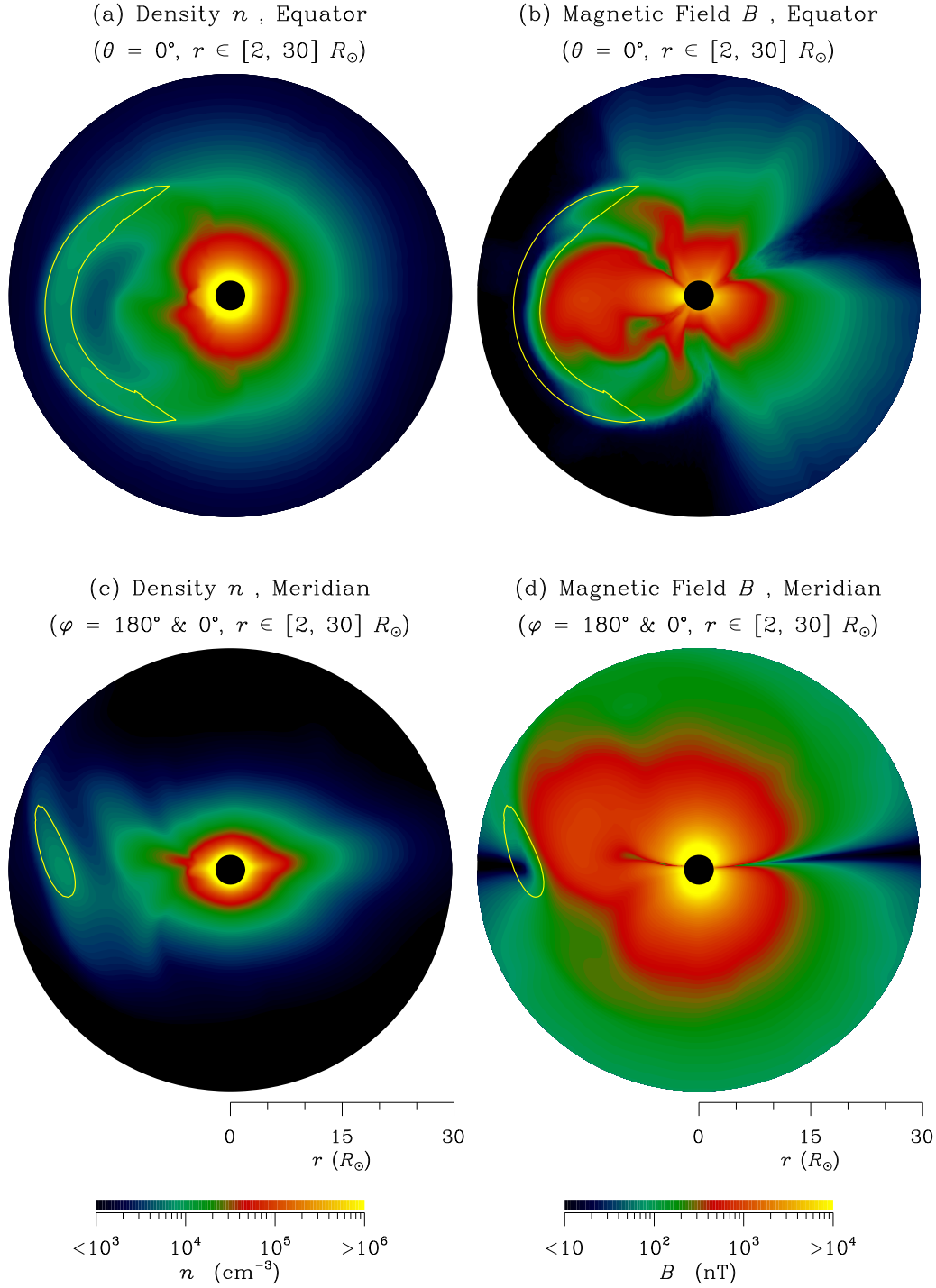


Figure 5. Distribution of proton density n (panels (a) and (c)) and magnetic field magnitude B (panels (b) and (d)) of the CME-disturbed solar wind in the corona, with the CME sheath enclosed by a solid yellow isocontour in each panel. Panels (a) and (b) correspond to the equatorial plane; panels (c) and (d) are in the plane of the central meridian as viewed in the FOV of $2\text{--}30 R_\odot$ from Earth.

accretion from the ambient solar wind downstream of the MFR-driven shock front is most pronounced near the ecliptic. Owing to such a pronounced snowplow effect, the 3D dome shape of the MFR-driven sheath gradually flattens (Figure 8). Because solar wind flows at solar minimum tend to be bimodal, with high-speed solar wind at high latitudes and slow-speed wind near the ecliptic, the sections of the MFR-driven sheath at high latitude tend to travel faster than the ecliptic portion. The morphology of the sheath front in the heliosphere is slightly

distorted, with a localized depression forming at ecliptic latitudes such that it is furthest from the Sun at high latitude (Figure 7(c)).

4. 2D Radiance Patterns of CMEs Viewed from an OOE Perspective

An MFR-driven CME can be continuously tracked in WL from its origin as a dark cavity in the low solar corona to its passage over a near-Earth spacecraft several days later.

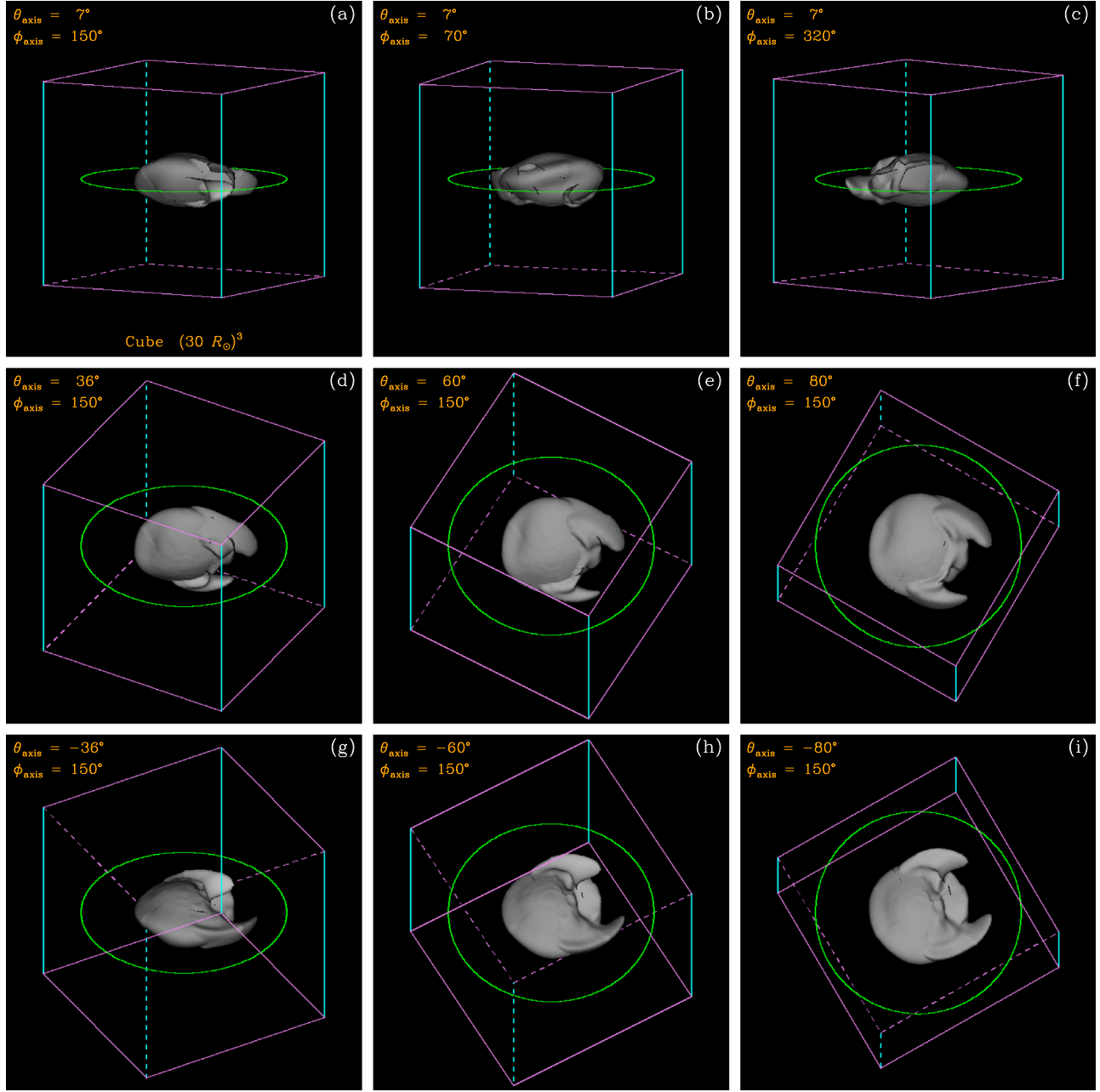


Figure 6. 3D isosurfaces of the CME-disturbed coronal density n as viewed from a number of different vantage points.

The unprecedented capability of *STEREO* has enabled continuous feature tracking through the corona and inner heliosphere. Hence, for the first time, an Earth-directed CME from the low corona that later impacts Earth can be tracked forward and backward in both time and space. The WL radiance at large elongations from the Sun depends on both the local electron density and the efficiency of the Thomson-scattering process. A propagating CME can be readily imaged by an observer at a wide range of viewing angles because the imaged radiance pattern viewed from a different perspective is contributed by a different part of the sheath front (Xiong et al. 2013a). The WL images of the CME studied in this paper are simultaneously captured by notional imagers located at various heliospheric latitudes $\theta_{s/c}$ and longitudes $\phi_{s/c}$. The radiance images of the CME in the corona and heliosphere are given in Figures 9 and 10,

respectively. In Figure 9, relative radiance enhancement $(I - I_0)/I_0$ is used to highlight the bright and transient CME front and suppress the relatively faint and stable emission from the background structures of coronal streamers and interplanetary CIRs. From any fixed $[\theta_{s/c}, \phi_{s/c}]$ perspective, one can identify the CME traveling through the high corona and the heliosphere as a moving radiance pattern in a 2D Sun-centered sky map (Figures 9 and 10). The WL patterns of the key anatomical elements of the CME are identified as a leading bright (dense) front corresponding to the sheath wall and a main dark (rarefied) cavity. Such a bright-dark (white-black) intensity contrast in the WL imagery of CMEs is crucial in their identification, because CME visibility in WL depends on the LOS integrated electron number density. The 3D dome-like density structure of the MFR-driven sheath extends to large distances ahead of the MFR itself. The

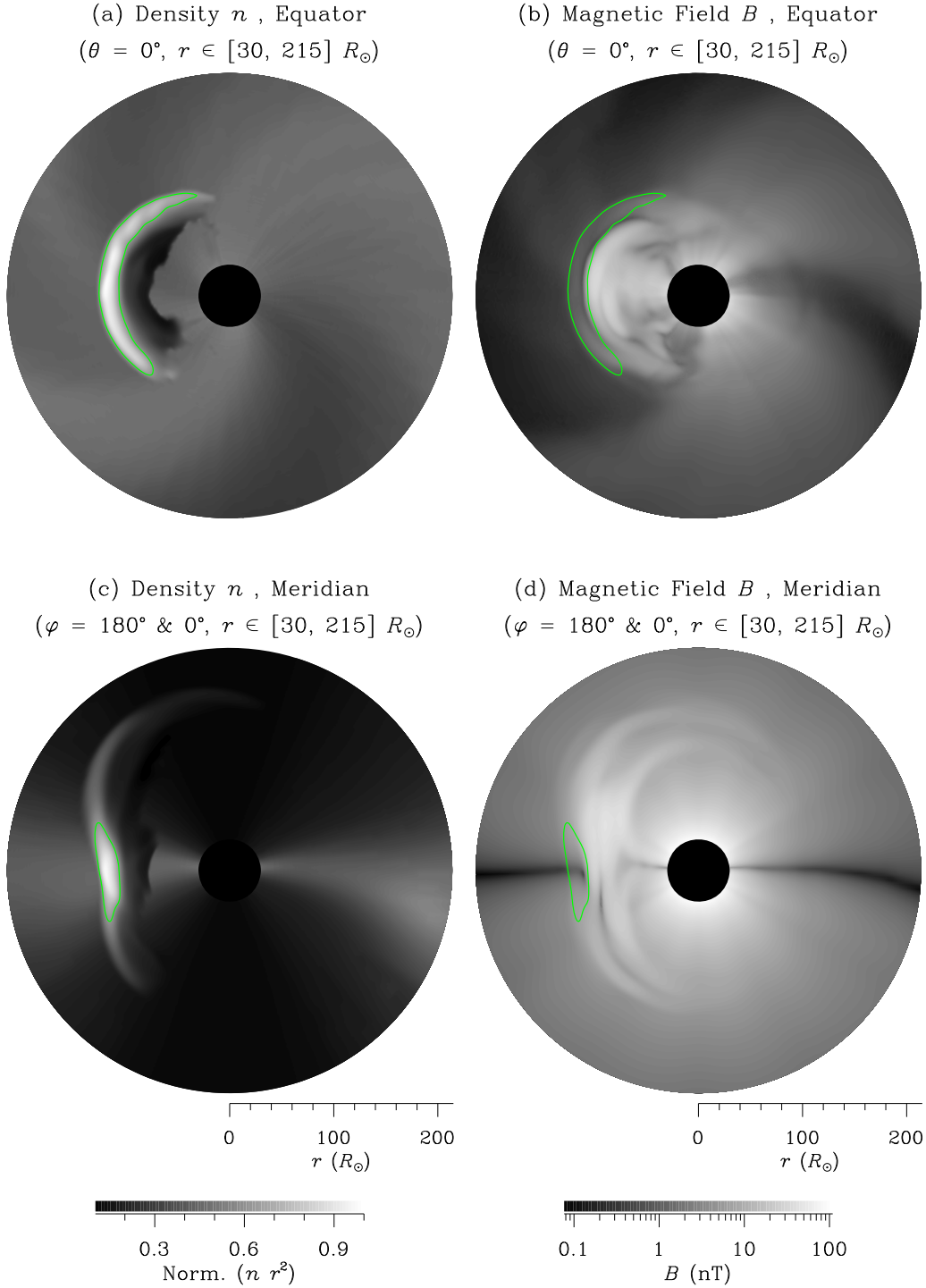


Figure 7. Same as Figure 5 but for a heliocentric distance range between 30 and 215 R_\odot .

longitudinal and latitudinal extent of the MFR-driven sheath is much larger than that of the MFR. The 2D radiance pattern of the sheath is highly dependent on viewpoint (Figures 9 and 10). The 2D WL image of the sheath viewed from an in-ecliptic viewpoint takes the form of a significantly distorted oval with north–south asymmetry and a localized sunward depression at ecliptic latitudes (Figures 9(a)–(c), 10(a)–(c)). In contrast, the sheath, as imaged from an OOE viewpoint, takes the form of a faint leading circle followed by a bright arc, which correspond to the wind sheath and coronal sheath

described in Section 3. The WL signature of the wind sheath is probably too weak to be visible in reality (Figures 9(g)–(i), 10(d)–(i)).

At solar minimum, the WL intensity of background CIRs is much weaker than that of typical CMEs. The CIR signatures in the coronal images (Figure 9) and heliospheric images (Figure 10) are much fainter in comparison with the bright CME sheath. Conversely, at solar maximum, it is difficult to image weak and narrow CMEs, in particular, in the presence of multiple long-lived foreground and background CIRs due to the

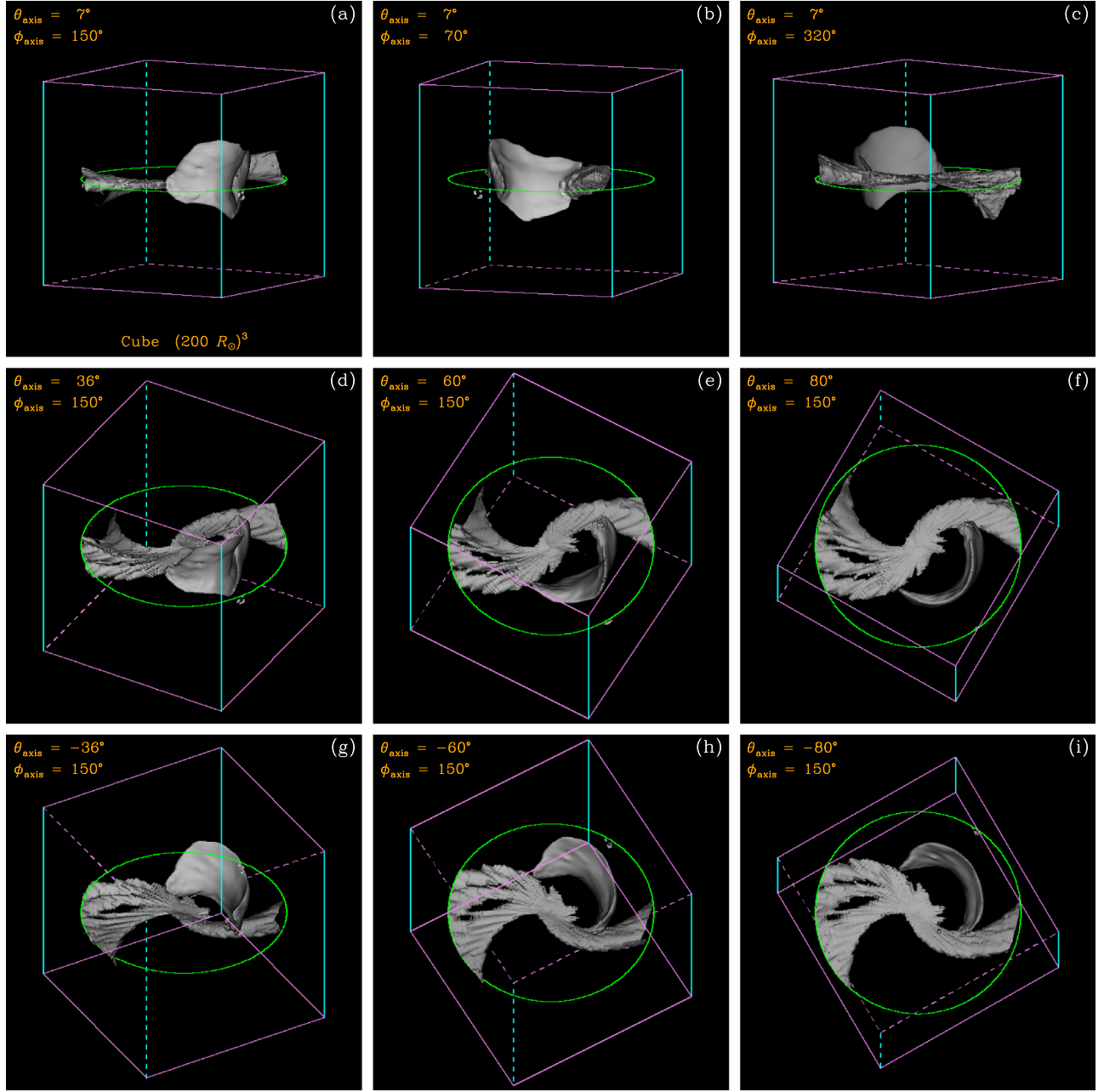


Figure 8. The 3D isosurfaces of the normalized CME-disturbed heliospheric density $n r^2$ as viewed from a number of different vantage points.

high intensity and complex morphology of the latter (Xiong et al. 2017). However, in general, a CME sheath is readily identified in WL imagery as a bright arc. Since the *SOHO* era, the appearance of a bright arc-shaped feature in the coronagraph imagery has been considered the forerunner of an ensuing CME and taken as confirmation of a previous solar EUV eruption.

The expanding wind sheath gradually fades during its propagation through the heliosphere, as demonstrated in Figure 11 for a fixed OOE viewing angle at $\theta_{s/c} = 60^\circ$ and $\phi_{s/c} = 150^\circ$. The MFR-driven sheath from an OOE viewpoint is generally brighter than that from an ecliptic perspective. The shape and intensity distribution of the WL image of the MFR-driven sheath is attributed to the bimodal nature of 3D solar wind flows at solar minimum. The section of the sheath that lies

in the fast solar wind is much faster and less compressed than that in the slow solar wind.

The longitudinal dimension of CMEs, which has up to now been integrated in WL imagery, can be resolved if imaged from an OOE viewpoint. The WL intensity of a propagating CME is jointly determined by its evolving CME mass distribution and the fixed Thomson-scattering geometry. A suite of WL imagers aboard a future OOE spacecraft would be highly advantageous in viewing near-ecliptic CMEs by (1) minimizing the limitations of the Thomson-scattering geometry and (2) enabling the large-scale longitudinal structure to be resolved. A bright sheath followed by a dark cavity is the most noticeable feature of such a CME in WL imagery from both near-ecliptic and OOE perspectives. The OOE imaging can further resolve the leading sheath into two

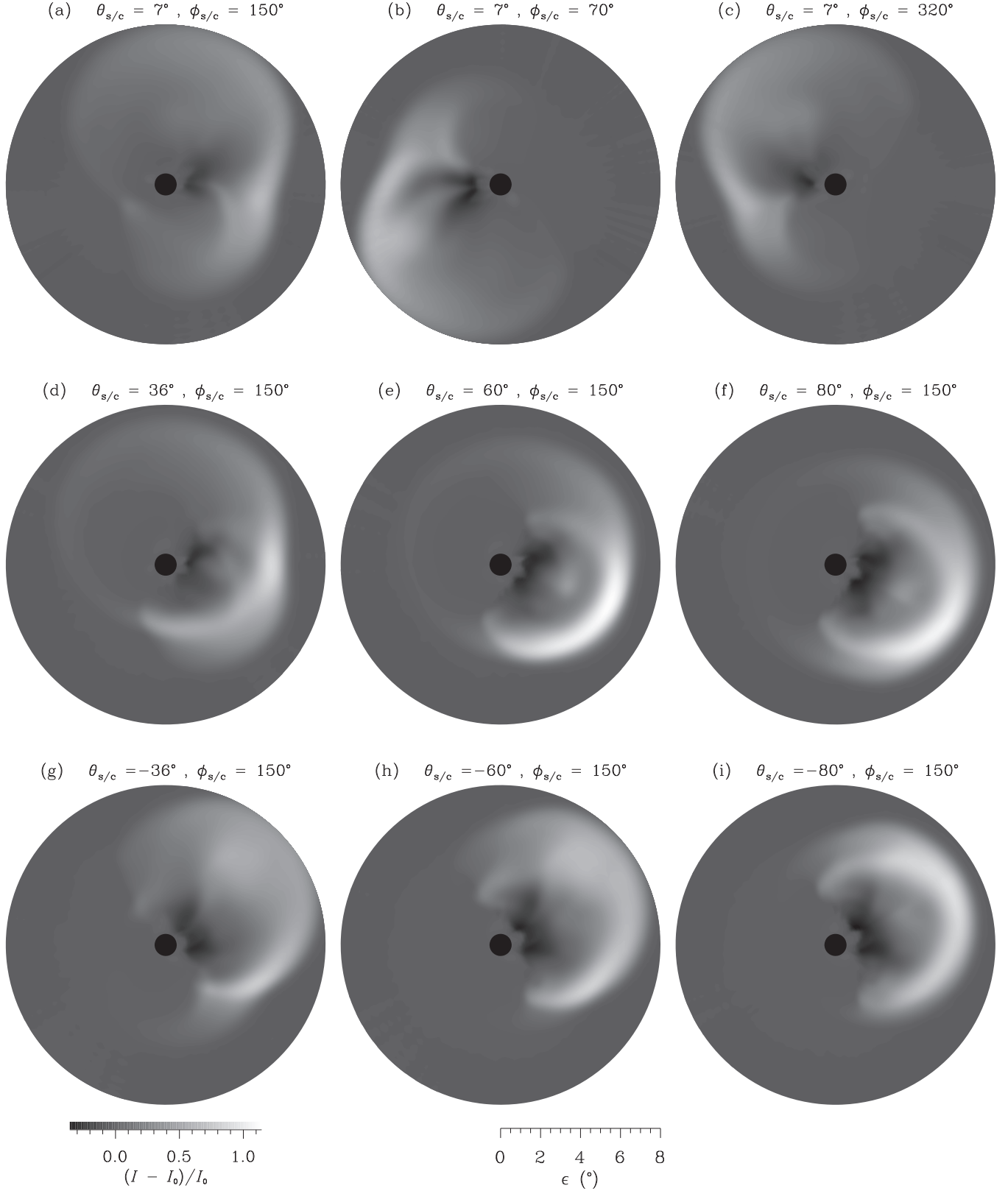
White-Light Corona Viewed from an Imager at $r_{s/c} = 215 R_{\odot}$ 

Figure 9. Relative radiance enhancement $(I - I_0)/I_0$ of the CME-disturbed corona over the elongation range $\epsilon \in [0^\circ, 8^\circ]$ as observed from the perspectives prescribed in Figure 6. Here I_0 refers to the background WL radiance before the CME eruption.

substructures: a circle-like wind sheath and an arc-like coronal sheath. As seen from a fixed OOE perspective in Figure 11, the WL intensity of the wind sheath gradually weakens, but, by

contrast, that of the coronal sheath remains conspicuous. The wind sheath would be manifest as a full halo around the Sun-centered occulting disk of a heliospheric imager. As the MFR thrusts

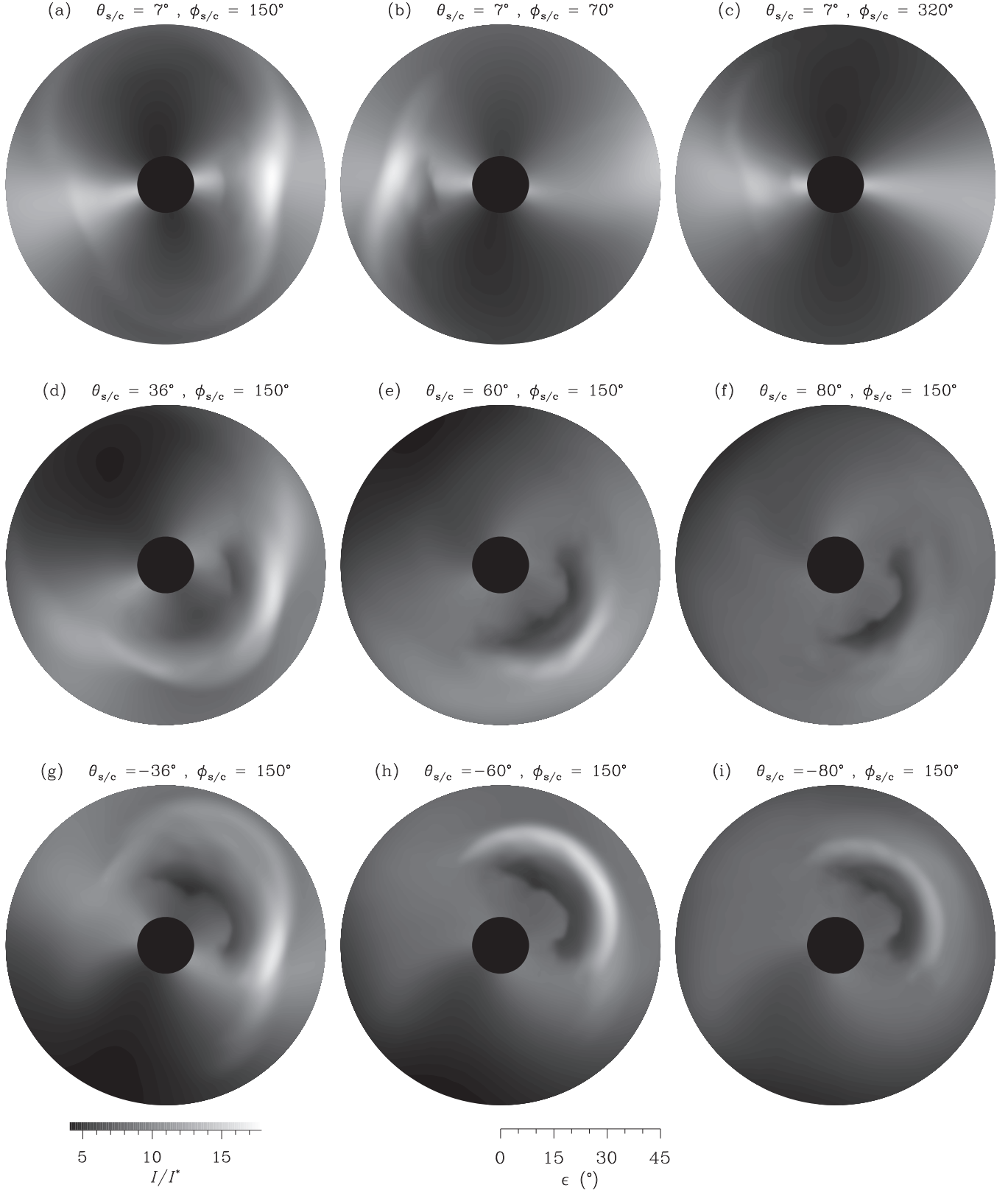
White-Light Sky Map Viewed from an Imager at $r_{s/c} = 215 R_{\odot}$ 

Figure 10. Normalized WL radiance I/I^* of the CME-disturbed heliosphere over the elongation range $\epsilon \in [8^\circ, 45^\circ]$, theoretically calculated for a number of different viewpoints defined in terms of $\theta_{s/c}$ and $\phi_{s/c}$ as prescribed in Figure 8.

through the center of the slow and dense solar wind emanating from coronal streamer boundaries, compression at its leading edge retards its ecliptic portion. The MFR-driven sheath gradually

assumes a concave-outward shape, and the MFR-driven CME abruptly decelerates. The leading dense, and hence bright, portion of the CME ahead of the MFR-related central cavity expands

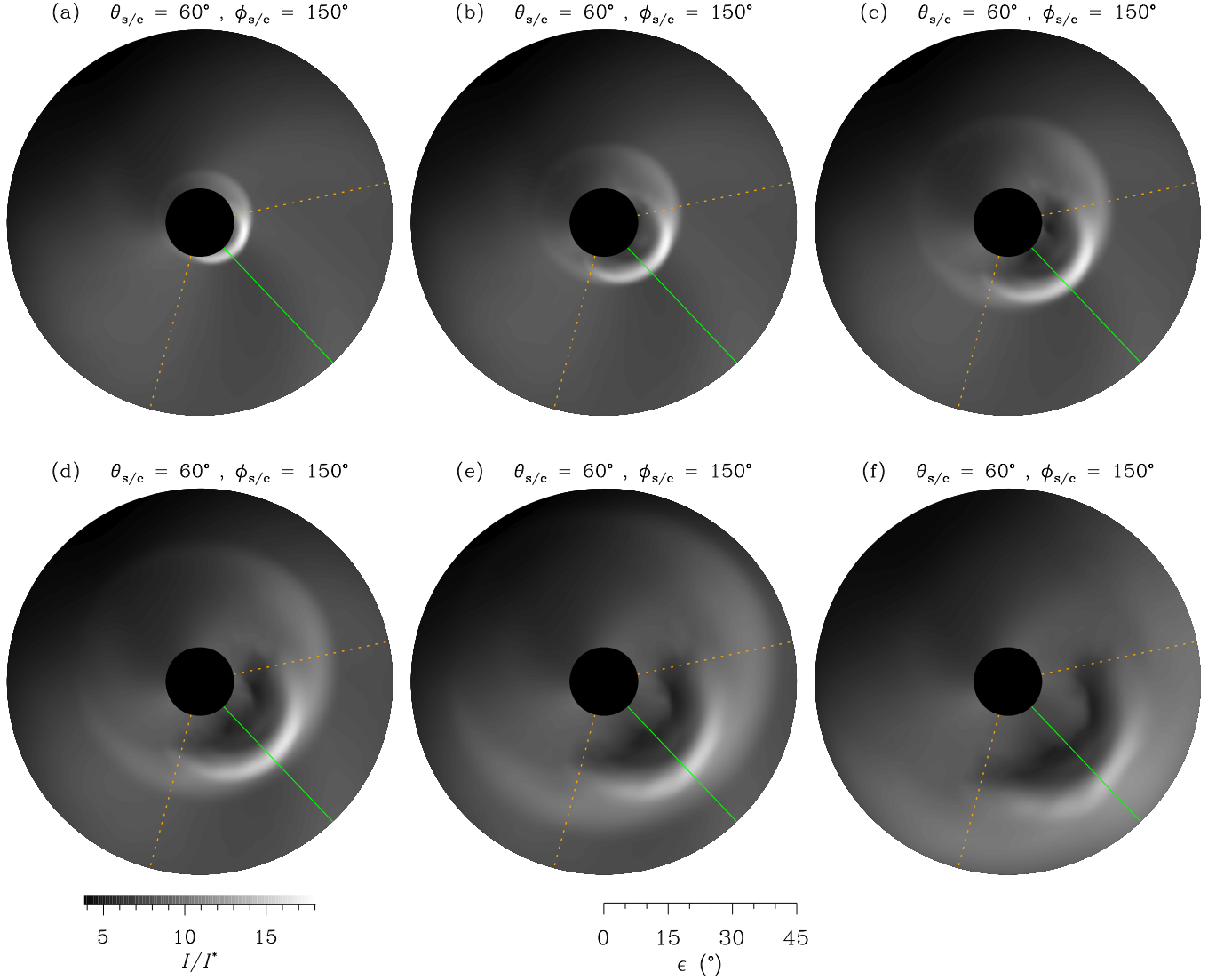
Interplanetary Propagating CME Viewed from an Imager at $r_{s/c} = 215 R_{\odot}$ and $\Delta t = 5$ hours

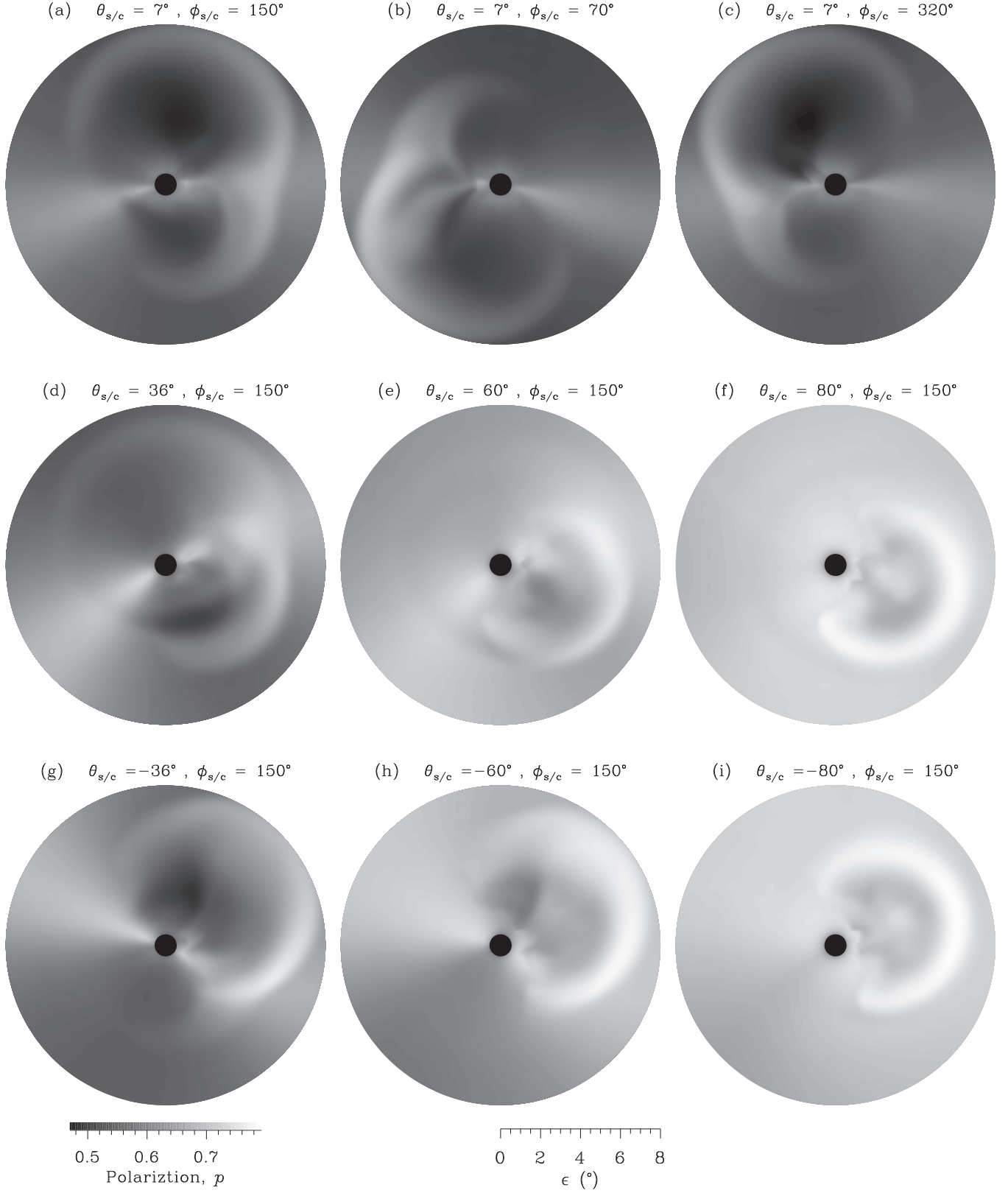
Figure 11. Normalized WL radiance I/I^* of the CME-disturbed heliosphere, calculated at a temporal cadence $\Delta t = 5$ hr from an OOE perspective of $\theta_{s/c} = 60^\circ$ and $\phi_{s/c} = 150^\circ$. The nose and flank edges of the CME are denoted by a solid line and two dashed lines, respectively.

rapidly as the CME propagates through the corona and thickens markedly as it travels through the inner heliosphere. In addition to changing shape, the CME accumulates mass as it propagates. The circular or near-circular radiance voids in WL imagery hint at the presence of mass-depleted MFR structures (DeForest et al. 2011, 2013). This reinforces the idea that heliospheric imagers and their postprocessing algorithms should be considered as unified systems (DeForest et al. 2011; DeForest & Howard 2015).

The high degree of polarization $p \geq 0.7$ of CME signatures from an OOE viewpoint (Figures 12–14) indicates that (1) the CME is almost located on or near the Thomson-scattering sphere and (2) the CME trajectory is close to the ecliptic. In fact, the favorable Thomson-scattering geometry (i.e., propensity for almost perpendicular scattering with its scattering angle $\chi \geq 70^\circ$) of an OOE vantage point when viewing near-ecliptic CMEs means that both total intensity and polarization degree of CME signatures are maximized from such an OOE perspective.

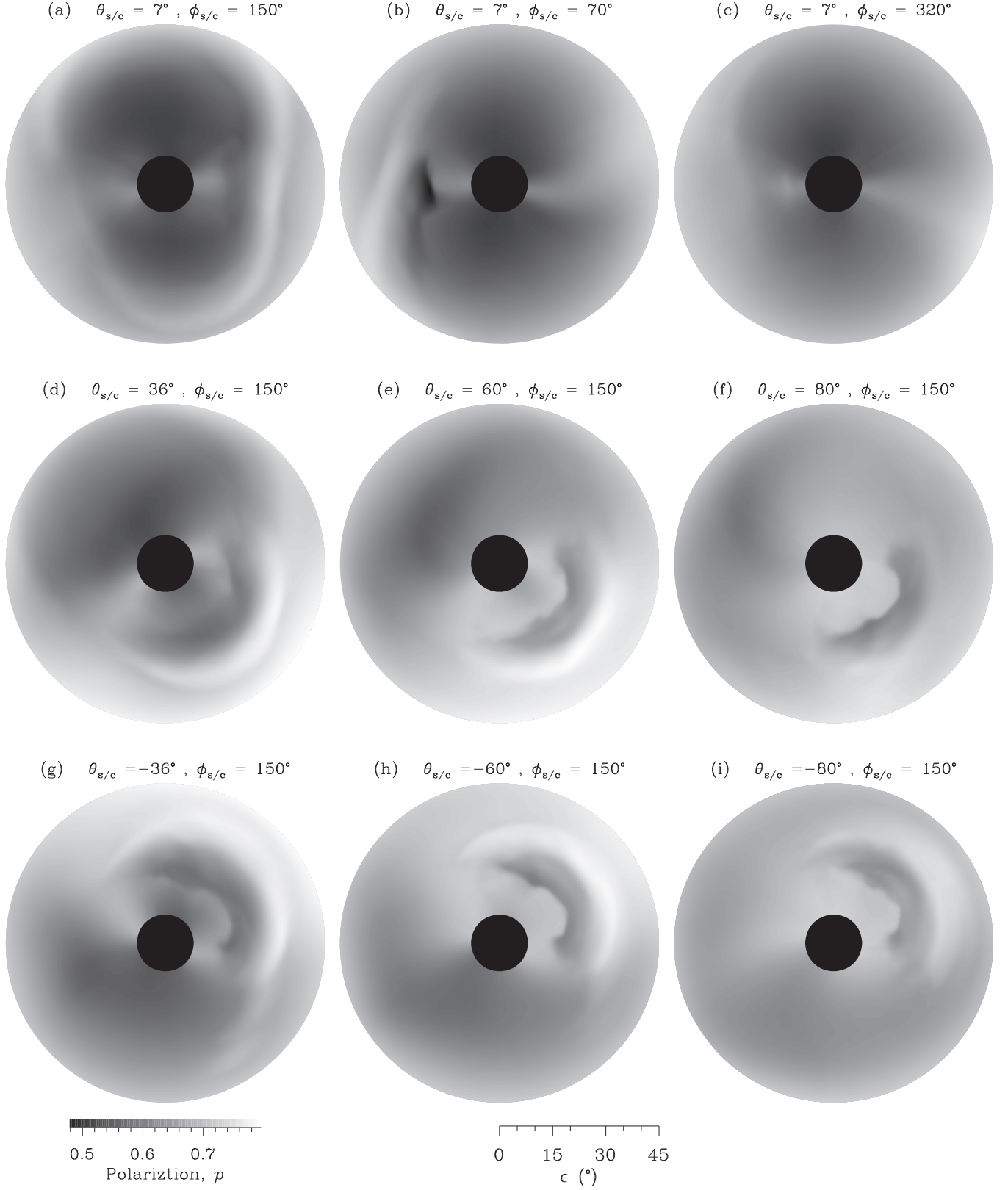
An Earth-directed MFR can be observed and identified as a cavity in OOE WL imagery and by identifying the characteristic signatures of an MC in near-Earth in situ measurements; i.e., a sheath cavity in interplanetary space and an MC at 1 au are both indicative of an MFR. The solid and dashed radial rays in Figures 11 and 14 delimit the longitudinal span and apex of the coronal sheath, respectively. For the CME studied in this paper, the front and apex of the coronal sheath are propagating radially outward without experiencing any longitudinal deviation. The CME studied here travels radially outward at a constant speed through interplanetary space. An OOE WL imager can continuously track the sheath front of a near-ecliptic CME and thus reliably measure the transporting speed of the CME.

Catalogs of CME events enable probabilities of CME acceleration/deceleration and deflection to be determined. Kinematically, there is a statistical tendency for fast CMEs to decelerate, whereas slow CMEs tend to accelerate

White-Light Corona Viewed from an Imager at $r_{s/c} = 215 R_{\odot}$ **Figure 12.** Same as Figure 9 but for the distribution of degree of polarization p .

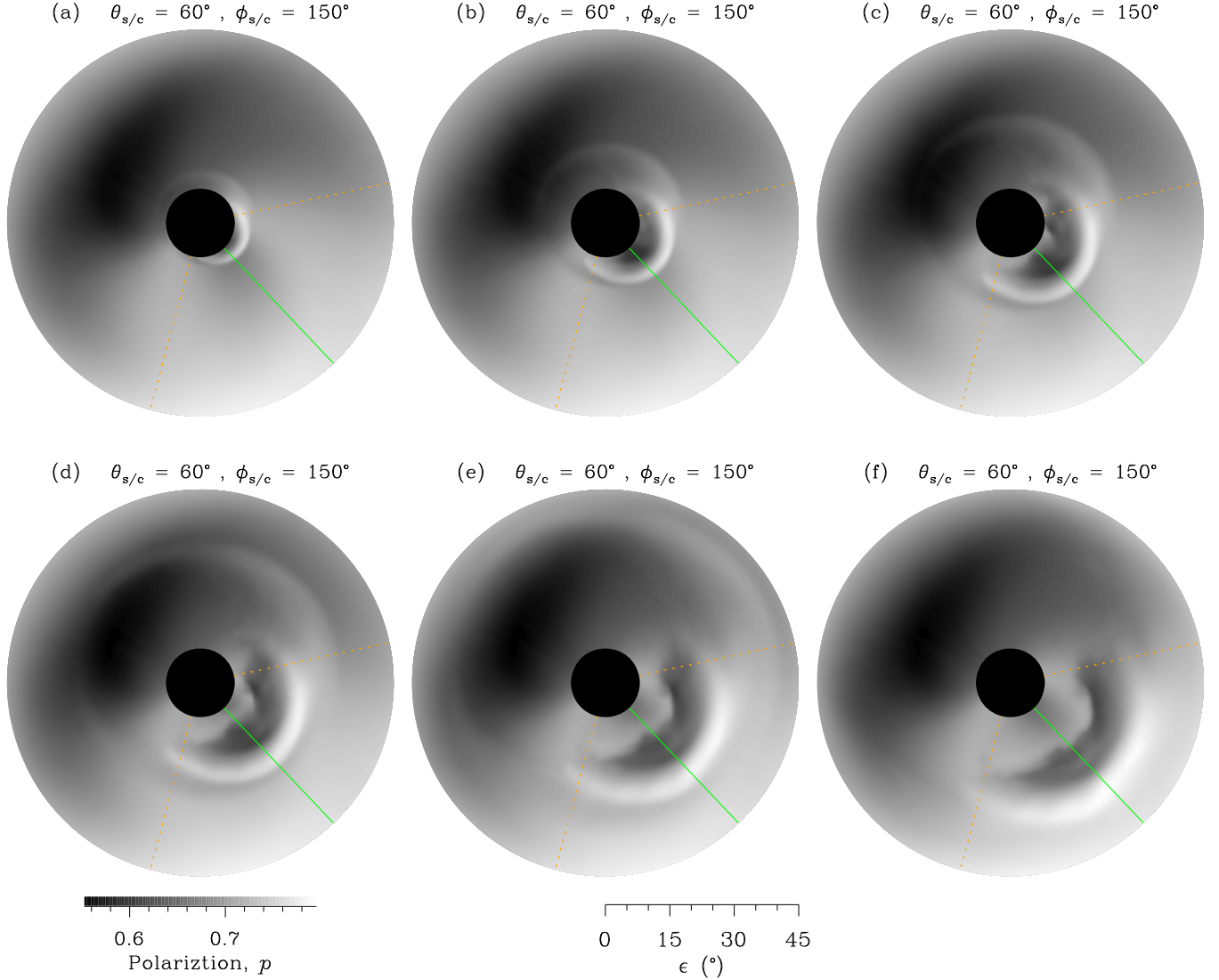
(Lindsay et al. 1999; Gopalswamy et al. 2001). The motion of an interplanetary CME is governed by two forces: a propelling Lorentz force and a retarding aerodynamic drag

force (Chen 1989; Vrřnak & Gopalswamy 2002; Cargill 2004). The Lorentz force decays rapidly with increasing heliocentric distance, implying that the drag is the dominant

White-Light Sky Map Viewed from an Imager at $r_{s/c} = 215 R_{\odot}$ **Figure 13.** Same as Figure 10 but for the distribution of degree of polarization p .

force for interplanetary CMEs. This accounts for the statistical tendency for CMEs to adjust their velocity to that of the ambient solar wind. Key questions relating to the competition

between Lorentz and drag forces acting on an interplanetary CME could be addressed quantitatively on the basis of OOE WL observations of near-ecliptic CME kinematics.

Interplanetary Propagating CME Viewed from an Imager at $r_{s/c} = 215 R_{\odot}$ and $\Delta t = 5$ hours**Figure 14.** Same as Figure 11 but for the distribution of degree of polarization p .

5. Discussion and Summary

In this paper, we synthesize the WL emission of a typical halo CME throughout its flight through the corona and heliosphere using the 3D numerical CESE-MHD model (Feng et al. 2010; Zhou et al. 2012) and classic Thomson-scattering theory (e.g., Billings 1966; Vourlidas & Howard 2006; Howard & Tappin 2009; Xiong et al. 2013a). Heliospheric WL imaging is mature in terms of its technology readiness level, given the successful operation of the space-borne *Coriolis*/SMEI and *STEREO*/HI instruments. To date, remote sensing of the corona and heliosphere, in WL or otherwise, has only been undertaken from an in-ecliptic perspective, which implies that each LOS (along which the signal is integrated) is near-parallel to the ecliptic plane. Hence, the longitudinal dimension of interplanetary CMEs and CIRs has, up to now, been integrated in WL imagery. As shown in Figures 9 and 10, the 2D radiance patterns of CMEs in WL sky maps look very different from different 3D viewpoints. The only OOE spacecraft, *Ulysses*, hosted no imaging instruments. The first OOE imaging of CMEs is expected to be realized by the forthcoming *Solo*

mission, due for launching in 2019. *Solo* will achieve a latitudinal inclination of 36° . As noted in other OOE mission concepts (SPI, POLARIS, SPORT, and InterHelioProbe), a prospective OOE WL imager in a solar polar orbit would permit the mapping of near-ecliptic large-scale density structures. Stereoscopic WL imaging of CMEs from both OOE and ecliptic spacecraft would provide the capability to unambiguously deconvolve the spatiotemporal variability of their large-scale WL emission into a 3D spatial distribution and a 1D temporal evolution.

A suite of WL imagers aboard a solar polar spacecraft would provide the context for in situ and remote-sensing observations by in-ecliptic spacecraft and imagery from ground-based telescopes. The panoramic FOV of an OOE imager could potentially encompass the ecliptic-orbiting spacecraft. Particle detectors can provide high-time-resolution in situ measurements of the solar wind plasma, including speed, mass flux, composition, magnetic field, and charge state (Gloeckler et al. 1995, 1998); suprathermal electron measurements can be used to infer magnetic connectivity of CMEs. DeForest et al. (2013), for example, identified the major anatomical elements



of the 2008 December 12 CME by combining remote-sensing observations with in situ measurements. More specifically, DeForest et al. (2013) analyzed (1) three key in situ solar wind parameters (density, magnetic field, and suprathermal electron pitch angle distribution), (2) the continuous remote-sensing imagery (Thomson-scattered WL) of the propagating CME, and (3) the topology of the pre-eruption coronal structure. The morphology of the cavity region imaged in WL by a coronagraph before and during CME eruption can aid understanding of CME initialization mechanisms such as the magnetic breakout, magnetic tether-cutting, kink and torus instabilities, and mass draining (cf. Table 1 of DeForest et al. 2013).




CME source locations on the Sun are statistically concentrated within two latitudinal belts of $|\theta| \in [15^\circ, 30^\circ]$ and essentially absent inside the polar regions of $|\theta| > 75^\circ$ (Wang et al. 2011). CMEs can be rotated, reconfigured, deformed, deflected, decelerated, and disguised during their journey through the ambient solar wind (Manchester et al. 2017 and references therein). In the low corona, CME deflection (the departure of a CME from a radial trajectory) is imposed through channeling by the background large-scale coronal magnetic field configuration (e.g., MacQueen et al. 1986; Kilpua et al. 2009; Shen et al. 2011; Möstl et al. 2015); in the heliosphere, such deflection is caused by interaction of the CME with the background solar wind (Wang et al. 2004, 2014) and other CMEs (Xiong et al. 2009; Lugaz et al. 2012). Longitudinal deflection of a CME may cause it to deviate away from the Sun–Earth line or toward it.

The WL radiance pattern of a CME propagating through the heliosphere can be used to infer its apparent trajectory. A WL view from an OOE vantage point can uncover how structures originating from coronal eruptions are connected to their far-removed interplanetary counterparts. Our case study of a typical halo CME at solar minimum provides an effective demonstration that OOE imaging in WL intensity (1) enables a CME to be tracked from its coronal initiation, (2) enables the course of a propagating CME front to be charted in the near-ecliptic POS, and (3) provides the capability to localize the CME sheath with additional WL polarization measurements. A panoramic OOE view in WL would be of tremendous benefit in terms of understanding interplanetary CME kinematics in the longitudinal dimension, with significant application to space weather prediction.

This work was jointly supported by the National Natural Science Foundation of China (41374175, 41231068, 41531073, 41627806, 41474150, 41274176, 41474149, 41674172, 41574171, and 41774157), the Specialized Research Fund for State Key Laboratories of China, the Strategic Priority Research Program on Space Science from the Chinese Academy of Sciences (XDA04060801), and the CAS/SAFEA International Partnership Program for Creative Research Teams. RAH and JAD were partly supported by the European Union Seventh Framework Programme (FP7/2007–2013) under grant agreement No. 606692 (HELcats). We sincerely thank the anonymous referee for constructive suggestions.

ORCID iDs

Ming Xiong (熊明)  <https://orcid.org/0000-0001-9427-7366>
Xueshang Feng
(冯学尚)  <https://orcid.org/0000-0001-8605-2159>

Lidong Xia (夏利东)  <https://orcid.org/0000-0001-8938-1038>
Bo Li (李波)  <https://orcid.org/0000-0002-7496-2734>
Keiji Hayashi (林啓志)  <https://orcid.org/0000-0001-9046-6688>

References

- Aly, J. J. 1984, *ApJ*, 283, 349
Amari, T., Luciani, J. F., Aly, J. J., Mikic, Z., & Linker, J. 2003, *ApJ*, 585, 1073
Antiochos, S. K., DeVore, C. R., & Klimchuk, J. A. 1999, *ApJ*, 510, 485
Appourchaux, T., Liewer, P., Watt, M., et al. 2009, *ExA*, 23, 1079
Billings, D. E. 1966, *A Guide to the Solar Corona* (San Diego, CA: Academic)
Brueckner, G. E., Delaboudiniere, J.-P., Howard, R. A., et al. 1998, *GeoRL*, 25, 3019
Brueckner, G. E., Howard, R. A., Koomen, M. J., et al. 1995, *SoPh*, 162, 357
Burlaga, L., Sittler, E., Mariani, F., & Schwenn, R. 1981, *JGR*, 86, 6673
Cargill, P. J. 2004, *SoPh*, 221, 135
Chen, J. 1989, *ApJ*, 338, 453
Chen, Y., Li, G. Q., & Hu, Y. Q. 2006, *ApJ*, 649, 1093
Cheng, X., Zhang, J., Liu, Y., & Ding, M. D. 2011, *ApJL*, 732, L25
Crooker, N. U., & Horbury, T. S. 2006, *SSRv*, 123, 93
Davies, J. A., Harrison, R. A., Perry, C. H., et al. 2012, *ApJ*, 750, 23
Davies, J. A., Harrison, R. A., Rouillard, A. P., et al. 2009, *GeoRL*, 36, L02102
Davis, C. J., Davies, J. A., Lockwood, M., et al. 2009, *GeoRL*, 36, L08102
DeForest, C. E., & Howard, T. A. 2015, *ApJ*, 804, 126
DeForest, C. E., Howard, T. A., & McComas, D. J. 2013, *ApJ*, 769, 43
DeForest, C. E., Howard, T. A., & Tappin, S. J. 2011, *ApJ*, 738, 103
Eyles, C. J., Harrison, R. A., Davis, C. J., et al. 2009, *SoPh*, 254, 387
Eyles, C. J., Simnett, G. M., Cooke, M. P., et al. 2003, *SoPh*, 217, 319
Feng, X., Ma, X., & Xiang, C. 2015, *JGRA*, 120, 10
Feng, X., Yang, L., Xiang, C., et al. 2010, *ApJ*, 723, 300
Forbes, T. G., Linker, J. A., Chen, J., et al. 2006, *SSRv*, 123, 251
Fox, N. J., Velli, M. C., Bale, S. D., et al. 2016, *SSRv*, 204, 7
Gibson, S. E., Kucera, T. A., Rastawicki, D., et al. 2010, *ApJ*, 724, 1133
Gibson, S. E., & Low, B. C. 1998, *ApJ*, 493, 460
Gloeckler, G., Balsiger, H., Bürgi, A., et al. 1995, *SSRv*, 71, 79
Gloeckler, G., Cain, J., Ipavich, F. M., et al. 1998, *SSRv*, 86, 497
Gopalswamy, N., Lara, A., Kaiser, M. L., & Bougeret, J.-L. 2001, *JGR*, 106, 25261
Gosling, J. T. 1990, *GMS*, 58, 343
Gosling, J. T., Bame, S. J., McComas, D. J., et al. 1994, *GeoRL*, 21, 1109
Gosling, J. T., McComas, D. J., Phillips, J. L., & Bame, S. J. 1991, *JGR*, 96, 7831
Gosling, J. T., Skoug, R. M., & Feldman, W. C. 2001, *GeoRL*, 28, 4155
Groth, C. P. T., De Zeeuw, D. L., Gombosi, T. I., & Powell, K. G. 2000, *JGR*, 105, 25053
Hammond, C. M., Crawford, G. K., Gosling, J. T., et al. 1995, *GeoRL*, 22, 1169
Harrison, R. A., Davis, C. J., Eyles, C. J., et al. 2008, *SoPh*, 247, 171
Howard, R. A., Brueckner, G. E., St. Cyr, O. C., et al. 1997, *GMS*, 99, 17
Howard, R. A., Moses, J. D., Vourlidas, A., et al. 2008, *SSRv*, 136, 67
Howard, T. A., & DeForest, C. E. 2012, *ApJ*, 752, 130
Howard, T. A., & Harrison, R. A. 2013, *SoPh*, 285, 269
Howard, T. A., & Tappin, S. J. 2009, *SSRv*, 147, 31
Hu, Q., & Sonnerup, B. U. Ö. 2002, *JGRA*, 107, 1142
Hundhausen, A. J. 1993, *JGRA*, 98, 13
Kaiser, M. L., Kucera, T. A., Davila, J. M., et al. 2008, *SSRv*, 136, 5
Kilpua, E. K. J., Pomoell, J., Vourlidas, A., et al. 2009, *AnGeo*, 27, 4491
Kuznetsov, V. D., Zelenyi, L. M., Zimovets, I. V., et al. 2016, *Ge&Ae*, 56, 781
Lepping, R. P., Berdichevsky, D. B., Wu, C.-C., et al. 2006, *AnGeo*, 24, 215
Lepping, R. P., Burlaga, L. F., & Jones, J. A. 1990, *JGR*, 95, 11957
Liewer, P. C., Ayon, J., Alexander, D., et al. 2008, in *NASA Space Science Vision Missions*, Vol. 224, ed. M. S. Allen (Reston, VA: American Institute of Aeronautics and Astronautics), 1
Lindsay, G. M., Luhmann, J. G., Russell, C. T., & Gosling, J. T. 1999, *JGR*, 104, 12515
Liu, Y., Davies, J. A., Luhmann, J. G., et al. 2010, *ApJL*, 710, L82
Liu, Y. D., Luhmann, J. G., Lugaz, N., et al. 2013, *ApJ*, 769, 45
Low, B. C. 2001, *JGR*, 106, 25141
Lugaz, N., Farrugia, C. J., Davies, J. A., et al. 2012, *ApJ*, 759, 68
MacQueen, R. M., Csoeke-Poekch, A., Hildner, E., et al. 1980, *SoPh*, 65, 91
MacQueen, R. M., Hundhausen, A. J., & Conover, C. W. 1986, *JGR*, 91, 31
Manchester, W., Kilpua, E. K. J., Liu, Y. D., et al. 2017, *SSRv*, 212, 1159
Manchester, W. B., Gombosi, T. I., Roussev, I., et al. 2004, *JGR*, 109, A02107
McComas, D. J., Barraclough, B. L., Funsten, H. O., et al. 2000, *JGR*, 105, 10419

- Mikic, Z., Barnes, D. C., & Schnack, D. D. 1988, *ApJ*, 328, 830
- Morgan, H., Byrne, J. P., & Habbal, S. R. 2012, *ApJ*, 752, 144
- Möstl, C., Rollett, T., Frahm, R. A., et al. 2015, *NatCo*, 6, 7135
- Möstl, C., Rollett, T., Lugaz, N., et al. 2011, *ApJ*, 741, 34
- Muller, D., Marsden, R. G., St Cyr, O. C., & Gilbert, H. R. 2013, *SoPh*, 285, 25
- Neugebauer, M., Forsyth, R. J., Galvin, A. B., et al. 1998, *JGR*, 103, 14587
- Neugebauer, M., Liewer, P. C., Smith, E. J., Skoug, R. M., & Zurbuchen, T. H. 2002, *JGRA*, 107, 1488
- Richardson, I. G., & Cane, H. V. 2004, *GeoRL*, 31, L18804
- Robbrecht, E., Patsourakos, S., & Vourlidas, A. 2009, *ApJ*, 701, 283
- Shen, C., Wang, Y., Gui, B., Ye, P., & Wang, S. 2011, *SoPh*, 269, 389
- St. Cyr, O. C., Plunkett, S. P., Michels, D. J., et al. 2000, *JGR*, 105, 18169
- Sturrock, P. A. 1991, *ApJ*, 380, 655
- Thernisien, A., Vourlidas, A., & Howard, R. A. 2009, *SoPh*, 256, 111
- Tóth, G., Sokolov, I. V., Gombosi, T. I., et al. 2005, *JGR*, 110, A12226
- Tousey, R. 1973, in *Space Research Conf. 2*, ed. M. J. Rycroft & S. K. Runcorn (Berlin: Akademie Verlag), 713
- Vourlidas, A., & Howard, R. A. 2006, *ApJ*, 642, 1216
- Vourlidas, A., Howard, R. A., Plunkett, S. P., et al. 2016, *SSRv*, 204, 83
- Vršnak, B., & Gopalswamy, N. 2002, *JGRA*, 107, 1019
- Vršnak, B., Maričić, D., Stanger, A. L., et al. 2007, *SoPh*, 241, 85
- Wang, Y., Chen, C., Gui, B., et al. 2011, *JGR*, 116, A04104
- Wang, Y., Shen, C., Wang, S., & Ye, P. 2004, *SoPh*, 222, 329
- Wang, Y., Wang, B., Shen, C., Shen, F., & Lugaz, N. 2014, *JGRA*, 119, 5117
- Wang, Y. M., Ye, P. Z., Wang, S., Zhou, G. P., & Wang, J. X. 2002, *JGRA*, 107, 1340
- Webb, D. F., & Howard, R. A. 1994, *JGR*, 99, 4201
- Wenzel, K. P., Marsden, R. G., Page, D. E., & Smith, E. J. 1992, *A&AS*, 92, 207
- Wu, J., Sun, W. Y., Zheng, J. H., et al. 2011, *AdSR*, 48, 943
- Xiong, M., Davies, J. A., Bisi, M. M., et al. 2013a, *SoPh*, 285, 369
- Xiong, M., Davies, J. A., Feng, X., et al. 2013b, *ApJ*, 777, 32
- Xiong, M., Davies, J. A., Li, B., et al. 2017, *ApJ*, 844, 76
- Xiong, M., Liu, Y., Liu, H., et al. 2016, *ChJSS*, 36, 245
- Xiong, M., Zheng, H., & Wang, S. 2009, *JGR*, 114, A11101
- Yashiro, S., Gopalswamy, N., Michalek, G., et al. 2004, *JGR*, 109, A07105
- Zhao, X. P., Hoeksema, J. T., & Scherrer, P. H. 2005, *JGR*, 110, A10101
- Zhou, Y. F., Feng, X. S., Wu, S. T., et al. 2012, *JGR*, 117, A01102